

Polar coordinate lattice Boltzmann modeling of compressible flows

Chuandong Lin¹, Aiguo Xu^{2*}, Guangcai Zhang², Yingjun Li^{1†}, Sauro Succi³

¹ *State Key Laboratory for GeoMechanics and Deep Underground Engineering,
China University of Mining and Technology, Beijing 100083, P.R.China*

² *National Key Laboratory of Computational Physics,
Institute of Applied Physics and Computational Mathematics,
P. O. Box 8009-26, Beijing 100088, P.R.China*

³ *Istituto Applicazioni Calcolo-CNR - Viale del Policlinico 137, 00161, Roma, Italy, EU*

(Dated: March 1, 2013)

* Corresponding author. E-mail address: Xu_Aiguo@iapcm.ac.cn

† Corresponding author. E-mail address: lyj@aphy.iphy.ac.cn

Abstract

We present a Polar Coordinate Lattice Boltzmann(PCLB) model for compressible flows. A method to evaluate the continuum distribution function from the discrete distribution function is indicated. Within the model, the temporal and spatial evolutions are treated with via the operator-splitting scheme. The temporal evolution is calculated analytically and the convection term is solved via a Modified Warming-Beam (MWB) scheme. Within the MWB scheme a suitable switch function is introduced. The new PCLB model works not only for subsonic flows but also for supersonic flows. It is validated and verified via the following well-known benchmark tests: (i) the rotational slip flow, (ii) the stable shock tube problem, (iii) the Richtmyer-Meshkov(RM) instability, (iv) the Kelvin-Helmholtz(KH) instability. As an original application, we studied the non-equilibrium characteristics of the system around three kinds of interfaces, the shock wave, the rarefaction wave and the material interface, for two specific cases. In one of the two cases, the material interface is initially perturbed and consequently the RM instability occurs. It is found that, the effects of deviating from thermodynamic equilibrium at the material interface differ significantly from those at the mechanical interfaces. The coupling effect of molecular motions in different degrees of freedom is much more pronounced at the material interface. The initial perturbation at the material interface enhances this coupling effect. The amplitude of deviations from equilibrium at the shock wave is much higher than those at the rarefaction wave and material interface. Our LB results confirm that the temperature increase first initiates the increase of internal kinetic energy in the degree of freedom corresponding to the direction of temperature gradient, then increases those in other degrees of freedom. By comparing each component of the high-order moments and its value in equilibrium, we can draw qualitative information on the actual distribution function. These results deepen our understanding of the mechanical and material interfaces from a more fundamental point of view, according to the distribution function in continuum velocity space, and provide valuable information to improve the physical modeling at a macroscopic level.

PACS numbers: 47.11.-j, 47.40.-x, 47.55.-t, 05.20.Dd

I. INTRODUCTION

During recent decades the lattice Boltzmann (LB) modeling and simulation have achieved great success in various complex flows [1]. However, most of these studies were focused on nearly incompressible flow, while with increasing the Mach number, the compressibility of flows has to be taken into account. Such high speed compressible flows are ubiquitous in aerophysics, astrophysics, explosion physics, medical physics and others. Given the great importance of shock waves in many fields of physics and engineering, constructing LB models for high speed compressible flows has attracted considerable interest since the early days of LB research [1].

In 1992 Alexander et al [2] formulated a compressible LB model for flows at high Mach number via introducing a flexible sound speed. This model works only for nearly isothermal compressible systems. In 1999 Yan et al [3] proposed a LB scheme for compressible Euler equations. In the years of 1998 and 2003 Sun and his coworker [4, 5] presented an adaptive LB scheme for the two- and three-dimensional systems, respectively. In this model the particle velocities vary with the Mach number and internal energy, so that the particle velocities are no longer constrained to fixed values. All of those models belong to the standard LB framework. However, due mainly to stability problems, to date, applications of LB methods to compressible flows remain scanty.

Besides the standard LB framework, the other way to formulate LB for high speed flows is to use the Finite-Difference (FD) scheme to calculate the temporal and spatial derivatives of the distribution function. In 1997 Cao et al [6] proposed to use the FD scheme to improve the numerical stability and apply nonuniform grids in the LB method. In the past decade, Tsutahara, Watari and Kataoka [7–11] proposed several nice FDLB models for the Euler and Navier-Stokes equations, where the discretizations in the space and in particle velocity are separated. In 2005 Xu [12, 13] extended the idea to handle binary fluids. However, similar to the case of standard LB models, these FDLB schemes only work for subsonic flows. For modeling and simulating high speed compressible flows, especially those with shocks, many attempts and considerable progress have been achieved [14–33].

It should be pointed out that, up to now, most of LB models for compressible fluids are based on the Cartesian coordinate system. In many cases the flows show divergent, convergent, and/or rotational behaviors, for example, in cylindrical or spherical devices. For

such flow systems, LB models based on polar coordinates, cylindrical coordinates or spherical coordinates are more convenient and are less exposed to numerical errors. There have been a number of LB methods based on curvilinear coordinates or for axisymmetric cylindrical coordinate system. Early in 1992, Nannelli and Succi [34] presented a general framework to extend the lattice Boltzmann equation to arbitrary lattice geometries. In this work, a finite-volume formulation of LB equation was given. Then some other finite-volume versions of the LB method were proposed for irregular meshes [35–39]. In 1997 He and Doolen [40] extended the LB method to apply to general curvilinear coordinate systems via using an interpolation-based strategy. In the following year Mei and Shyy [41] developed a FDLB method in body-fitted curvilinear coordinates with non-uniform grids. Later, Halliday et al [42] proposed a Polar Coordinate Lattice Boltzmann(PCLB) method for hydrodynamics. In 2005 Premnath and Abraham [43] presented a LB model for axisymmetric multiphase flows. In this work source terms were added to a two-dimensional standard LB equation for multiphase flows such that the emergent dynamics can be transformed into the axisymmetric cylindrical coordinate system. But all those LB methods work only for isothermal and nearly incompressible flows. In 2010 Asinari et al [44] formulated a LB scheme to analyze the radiative heat transfer problems in a participation medium, but did not take into account the effects of fluid flow. In 2011 Watari [45] formulated a polar coordinate FDLB scheme to investigate the rotational slip flow problems in coaxial cylinders. This work presents valuable information on the LB application to the cylindrical system. However, this model works also only for subsonic compressible flow systems. In the present work we extend the FDLB model based on polar coordinates to compressible flow systems with high Mach number so that it can be used to simulate flows with shock waves.

The rest of the paper is structured as follows. In section II we first review the polar FDLB model by Watari, then present our contributions for the polar FDLB model. The latter includes the operator-splitting scheme, the analytical solution for the temporal evolution and the Modified Warming-Beam(MWB) scheme for the convection behavior. Section III is for the validation and verification of the new LB model. In section IV we study the non-equilibrium characteristics of the system in two special cases related to shock wave passing material interfaces. The method to qualitatively recover the actual distribution function is illustrated. Section V concludes the present paper.

II. POLAR FDLB MODEL

A. Brief review of Watari model

Below is a general description of the two-dimensional FDLB thermal model [45], which is applicable to both rectangular cartesian coordinate system and polar coordinate system. The evolution of the distribution function f_{ki} with the Bhatanger-Gross-Krook approximation [46] reads,

$$\frac{\partial f_{ki}}{\partial t} + \mathbf{v}_{ki} \cdot \nabla f_{ki} = -\frac{1}{\tau} [f_{ki} - f_{ki}^{eq}] \quad (1)$$

where f_{ki} (f_{ki}^{eq}) is the discrete (equilibrium) distribution function; τ is the relaxation time determining the speed of approaching equilibrium; \mathbf{v}_{ki} is the discrete velocity which will be defined below. The original Discrete-Velocity-Model(DVM) by Watari and Tsutahara is composed of $N_k + 1$ groups of discrete velocities. The k -th group has the size v_k . Each group has N_i components distributed in N_i directions. Mathematically, the DVM can be write as:

$$\mathbf{v}_{ki} = \sum_{\alpha} v_{ki\alpha} \mathbf{e}_{\alpha} = v_{kix} \mathbf{e}_x + v_{kiy} \mathbf{e}_y, \quad (2)$$

where $v_{kix} = v_k \cos[2\pi(i-1)/N_i]$, $v_{kiy} = v_k \sin[2\pi(i-1)/N_i]$, \mathbf{e}_x and \mathbf{e}_y are the unit vectors in the two-dimensional rectangular cartesian coordinate system, $k = 0, 1, 2, \dots, N_k$, and $i = 1, 2, \dots, N_i$. In this work we discuss the polar coordinate FDLB model for fixed $N_k = 4$ and flexible N_i . The sizes of discrete velocities are chosen as $v_0 = 0$, $v_1 = 1$, $v_2 = 2.92$, $v_3 = 2.99$, $v_4 = 4.49$. The sketches of the DVM for cases of $N_i = 8$, $N_i = 16$, $N_i = 24$ are shown in Fig.1.

It's easy to prove that this DVM with $N_i = 8$ has at least up to seventh rank isotropy[21]. The macroscopic quantities are defined as

$$\rho = \sum_{ki} f_{ki}^{eq} = \sum_{ki} f_{ki}, \quad (3)$$

$$\rho \mathbf{u} = \sum_{ki} f_{ki}^{eq} \mathbf{v}_{ki} = \sum_{ki} f_{ki} \mathbf{v}_{ki}, \quad (4)$$

$$\rho E = \sum_{ki} \frac{1}{2} f_{ki}^{eq} (\mathbf{v}_{ki} - \mathbf{u}) \cdot (\mathbf{v}_{ki} - \mathbf{u}) = \sum_{ki} \frac{1}{2} f_{ki} (\mathbf{v}_{ki} - \mathbf{u}) \cdot (\mathbf{v}_{ki} - \mathbf{u}). \quad (5)$$

Here ρ , \mathbf{u} ($= u_r \mathbf{e}_r + u_{\theta} \mathbf{e}_{\theta} = u_x \mathbf{e}_x + u_y \mathbf{e}_y$), P ($= \rho T$), E ($= T/(\gamma - 1)$) are the hydrodynamic density, flow velocity, pressure and internal kinetic energy per unit mass, respectively; T is

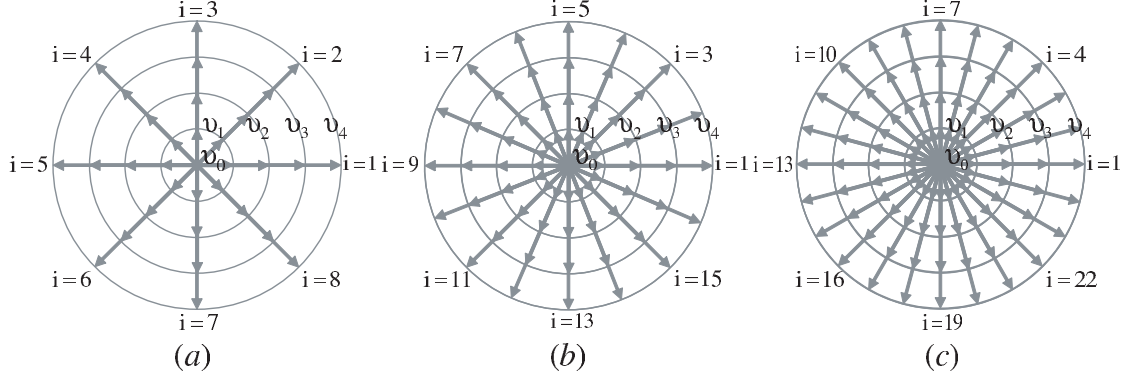


FIG. 1: Sketches of DVM with fixed $N_k = 4$ and various values of N_i . (a) $N_i = 8$. (b) $N_i = 16$. (c) $N_i = 24$.

the temperature and $\gamma (= 2)$ is the specific-heat ratio. Other velocity moments that the local equilibrium distribution function has to satisfy are:

$$\sum_{ki} f_{ki}^{eq} \mathbf{v}_{ki} \mathbf{v}_{ki} = \rho(E\mathbf{I} + \mathbf{u}\mathbf{u}), \quad (6)$$

$$\sum_{ki} f_{ki}^{eq} \mathbf{v}_{ki} \mathbf{v}_{ki} \mathbf{v}_{ki} = \rho[E(\mathbf{u}_\alpha \mathbf{e}_\beta \mathbf{e}_\gamma \delta_{\beta\gamma} + \mathbf{e}_\alpha \mathbf{u}_\beta \mathbf{e}_\gamma \delta_{\gamma\alpha} + \mathbf{e}_\alpha \mathbf{e}_\beta \mathbf{u}_\gamma \delta_{\alpha\beta}) + \mathbf{u}\mathbf{u}\mathbf{u}], \quad (7)$$

$$\sum_{ki} \frac{1}{2} f_{ki}^{eq} \mathbf{v}_{ki} \cdot \mathbf{v}_{ki} \mathbf{v}_{ki} = \rho(E\mathbf{I} + \mathbf{u}\mathbf{u}), \quad (8)$$

$$\sum_{ki} \frac{1}{2} f_{ki}^{eq} \mathbf{v}_{ki} \cdot \mathbf{v}_{ki} \mathbf{v}_{ki} \mathbf{v}_{ki} = \rho(2E + \frac{1}{2} \mathbf{u} \cdot \mathbf{u})(E\mathbf{I} + \mathbf{u}\mathbf{u}), \quad (9)$$

where \mathbf{I} is the unit tensor, $\mathbf{v}_{ki} \mathbf{v}_{ki}$ and $\mathbf{u}\mathbf{u}$ are double dyadics, $\mathbf{v}_{ki} \mathbf{v}_{ki} \mathbf{v}_{ki}$ and $\mathbf{u}\mathbf{u}\mathbf{u}$ are triple dyadics.

The equilibrium distribution function f_{ki}^{eq} is computed by,

$$f_{ki}^{eq} = \rho F_k \left[\left(1 - \frac{u^2}{2E} + \frac{u^4}{8E^2}\right) + \frac{v_{ki\varepsilon} u_\varepsilon}{E} \left(1 - \frac{u^2}{2E}\right) + \frac{v_{ki\varepsilon} v_{ki\pi} u_\varepsilon u_\pi}{2E^2} \left(1 - \frac{u^2}{2E}\right) + \frac{v_{ki\varepsilon} v_{ki\pi} v_{ki\vartheta} u_\varepsilon u_\pi u_\vartheta}{6E^3} + \frac{v_{ki\varepsilon} v_{ki\pi} v_{ki\vartheta} v_{ki\xi} u_\varepsilon u_\pi u_\vartheta u_\xi}{24E^4} \right] \quad (10)$$

where the weighting coefficients are calculated in the following way,

$$F_k = \frac{1}{v_k^2 (v_k^2 - v_{k+1}^2) (v_k^2 - v_{k+2}^2) (v_k^2 - v_{k+3}^2)} [B_4 E^4 + B_3 (v_{k+1}^2 + v_{k+2}^2 + v_{k+3}^2) E^3 + B_2 (v_{k+1}^2 v_{k+2}^2 + v_{k+2}^2 v_{k+3}^2 + v_{k+3}^2 v_{k+1}^2) E^2 + B_1 v_{k+1}^2 v_{k+2}^2 v_{k+3}^2 E], \quad (11a)$$

$$F_0 = 1/B_0 - (F_1 + F_2 + F_3 + F_4), \quad (11b)$$

TABLE I: Coefficients B_0, B_4, B_3, B_2, B_1 for each model

model	N_i	B_0	B_4	B_3	B_2	B_1
Octagon	8	8	48	-6	1	$-\frac{1}{4}$
Double Octagon	16	16	24	-3	$\frac{1}{2}$	$-\frac{1}{8}$
Triple Octagon	24	24	16	-2	$\frac{1}{3}$	$-\frac{1}{12}$

$$\{k+l\} = \begin{cases} k+l & \text{if } k+l \leq 4 \\ k+l-4 & \text{if } k+l > 4 \end{cases}.$$

And the coefficients B_0, B_4, B_3, B_2, B_1 for each model are summarized in Table I.

The temporal and spatial derivatives in Eq.(1) are computed by the FD schemes. Via the Chapman-Enskog expansion it is easy to find that the above FDLB model presents the same results as the following Navier-Stokes equations

$$\frac{\partial \rho}{\partial t} + \nabla \cdot (\rho \mathbf{u}) = 0, \quad (12)$$

$$\frac{\partial(\rho \mathbf{u})}{\partial t} + \nabla \cdot (P \mathbf{I} + \rho \mathbf{u} \mathbf{u}) + \nabla \cdot [\mu(\nabla \cdot \mathbf{u}) \mathbf{I} - \mu(\nabla \cdot \mathbf{u}) \mathbf{I}] = 0, \quad (13)$$

$$\begin{aligned} & \frac{\partial}{\partial t}(\rho E + \frac{1}{2} \rho u^2) + \nabla \cdot [\rho \mathbf{u} (E + \frac{1}{2} u^2 + \frac{P}{\rho})] \\ & - \nabla \cdot [\kappa' \nabla E + \mu \mathbf{u} \cdot (\nabla \mathbf{u}) - \mu \mathbf{u} (\nabla \cdot \mathbf{u}) + \frac{1}{2} \mu \nabla u^2] = 0, \end{aligned} \quad (14)$$

in the hydrodynamic limit, where μ and κ' are viscosity and heat conductivity, respectively. They are related to the pressure P and relaxation time τ via

$$\kappa' = 2\mu = 2P\tau. \quad (15)$$

B. Our contribution

1. Operator-splitting scheme

Equation (1) could be written in the following scalar form in polar coordinates

$$\frac{\partial f_{ki}}{\partial t} + v_{kir} \frac{\partial f_{ki}}{\partial r} + \frac{1}{r} v_{ki\theta} \frac{\partial f_{ki}}{\partial \theta} = -\frac{1}{\tau} [f_{ki} - f_{ki}^{eq}]. \quad (16)$$

To present our new scheme, we first decompose the two-dimensional FDLB Eq. (16) into the following one-dimensional form

$$\begin{cases} \frac{\partial f_{ki}}{\partial t} = -\frac{1}{\tau} [f_{ki} - f_{ki}^{eq}] \\ \frac{\partial f_{ki}}{\partial t} + v_{kir} \frac{\partial f_{ki}}{\partial r} = 0 \\ \frac{\partial f_{ki}}{\partial t} + \frac{1}{r} v_{ki\theta} \frac{\partial f_{ki}}{\partial \theta} = 0 \end{cases} \quad (17)$$

via the operator splitting scheme.

2. Analytic solution for temporal evolution

The first subequation in Eq.(17) has a traditional discrete solution in the following form

$$f_{ki}^{t+\Delta t} = f_{ki}^t - \frac{\Delta t}{\tau} (f_{ki}^t - f_{ki}^{eq}) \quad (18)$$

In fact the subequation can be given an analytical solution dynamically as below

$$f_{ki}^{t+dt} = \exp(-\frac{dt}{\tau}) [f_{ki}^t - f_{ki}^{eq} + f_{ki}^{eq} \exp(\frac{dt}{\tau})] \quad (19)$$

Comparing with the Eq.(18), Eq.(19) gives an accurate solution, which is very helpful when the term $\frac{\Delta t}{\tau}$ or $(f_{ki}^t - f_{ki}^{eq})$ is not small enough.

3. MWB scheme for spatial evolution

The last two subequations in Eq.(17) can be written uniformly as

$$\begin{aligned} \frac{\partial \psi}{\partial t} + a \frac{\partial \psi}{\partial \xi} &= 0 \\ \psi &\rightarrow f_{ki} \\ \xi &\rightarrow r \text{ or } \theta \\ a &\rightarrow v_{kir} \text{ or } \frac{1}{r} v_{ki\theta}. \end{aligned} \quad (20)$$

Since v_{kir} is a constant and r can also be regarded as a constant when consider the last subequation of Eq.(17), we can further obtain

$$\frac{\partial^2 \psi}{\partial t^2} - a^2 \frac{\partial^2 \psi}{\partial \xi^2} = 0. \quad (21)$$

By introducing the symbol, $\psi(\xi_j, t_n) = \psi_j^n$, and performing the Taylor expansion, we get

$$\psi_j^{n+1} = \psi_j^n - a \Delta t \left(\frac{\partial \psi}{\partial \xi} \right)_j^n + \frac{1}{2} a^2 \Delta t^2 \left(\frac{\partial^2 \psi}{\partial \xi^2} \right)_j^n + O(\Delta t^3). \quad (22)$$

The derivatives about ξ_j in Eq.(22) are all calculated by using the second order upwind scheme,

$$\left(\frac{\partial\psi}{\partial\xi}\right)_j^n = \begin{cases} \frac{3\psi_j^n - 4\psi_{j-1}^n + \psi_{j-2}^n}{2\Delta\xi} + O(\Delta\xi^2) & \text{if } a \geq 0 \\ -\frac{3\psi_j^n - 4\psi_{j+1}^n + \psi_{j+2}^n}{2\Delta\xi} + O(\Delta\xi^2) & \text{if } a < 0 \end{cases} \quad (23)$$

$$\left(\frac{\partial^2\psi}{\partial\xi^2}\right)_j^n = \begin{cases} \frac{\psi_j^n - 2\psi_{j-1}^n + \psi_{j-2}^n}{\Delta\xi^2} + O(\Delta\xi) & \text{if } a \geq 0 \\ \frac{\psi_j^n - 2\psi_{j+1}^n + \psi_{j+2}^n}{\Delta\xi^2} + O(\Delta\xi) & \text{if } a < 0 \end{cases} \quad (24)$$

Thus, from Eq.(22) we get the well-known Warming-Beam Scheme,

$$\psi_j^{n+1} = \begin{cases} \psi_j^n - C(\psi_j^n - \psi_{j-1}^n) - \frac{1}{2}C(1-C)(\psi_j^n - 2\psi_{j-1}^n + \psi_{j-2}^n) & \text{if } a \geq 0 \\ \psi_j^n - C(\psi_{j+1}^n - \psi_j^n) + \frac{1}{2}C(1+C)(\psi_j^n - 2\psi_{j+1}^n + \psi_{j+2}^n) & \text{if } a < 0 \end{cases} \quad (25)$$

where the higher order tiny quantities have been omitted, $C = a\Delta t/\Delta\xi$ is the Courant-number. The Stability condition requires $|C| \leq 1$.

In this work we modify the Warming-Beam scheme. Firstly, Eq.(25) is written as

$$\psi_j^{n+1} = \psi_j^n - [C + \frac{1}{2}C(1 - |C|)(1 - \eta)]\delta \quad (26)$$

where

$$\delta = \begin{cases} \psi_j^n - \psi_{j-1}^n & \text{if } 0 \leq C \leq 1 \\ \psi_{j+1}^n - \psi_j^n & \text{if } -1 \leq C < 0 \end{cases} \quad (27)$$

$$\eta = \begin{cases} \frac{\psi_{j-1}^n - \psi_{j-2}^n}{\psi_j^n - \psi_{j-1}^n} & \text{if } \psi_j^n \neq \psi_{j-1}^n \text{ and } a \geq 0 \\ \text{const} & \text{if } \psi_j^n = \psi_{j-1}^n \text{ and } a \geq 0 \\ \frac{\psi_{j+2}^n - \psi_{j+1}^n}{\psi_{j+1}^n - \psi_j^n} & \text{if } \psi_{j+1}^n \neq \psi_j^n \text{ and } a < 0 \\ \text{const} & \text{if } \psi_{j+1}^n = \psi_j^n \text{ and } a < 0 \end{cases} \quad (28)$$

Then, by introducing a switch function $S(\eta)$, Eq.(26) is written as

$$\psi_j^{n+1} = \psi_j^n - [C + \frac{1}{2}C(1 - |C|)(1 - S(\eta))(1 - \eta)]\delta \quad (29)$$

To make the scheme monotonous in space, we require

$$0 \leq \varphi(C) \leq 1, \quad (30)$$

where $\varphi(C)$ is a quadratic polynomial function

$$\varphi(C) = |C| + \frac{1}{2}|C|(1 - |C|)(1 - S(\eta))(1 - \eta) \quad (31)$$

From Eqs.(30)-(31) we get

$$\begin{cases} \varphi(0) = 0 \\ 0 \leq \varphi(C) \leq 1 \\ \varphi(1) = \varphi(-1) = 1. \end{cases} \quad (32)$$

Equation (31) can be written as

$$\psi(x) = x + \frac{1}{2}x(1-x)\alpha \quad (33)$$

where $x = |C|$, $\psi(x) = \varphi(C)$, $\alpha = (1 - S(\eta))(1 - \eta)$. Thus, Eq.(32) becomes

$$\begin{cases} \psi(0) = 0 \\ 0 \leq \psi(x) \leq 1 \\ \psi(1) = 1. \end{cases} \quad (34)$$

Equation (33) describes a parabola which has a extremum value at

$$x_e = \frac{1}{2} + \frac{1}{\alpha}. \quad (35)$$

To satisfy all the three conditions in Eq.(34), we require

$$x_e \geq 1 \text{ or } x_e \leq 0 \quad (36)$$

From the conditions in Eq.(36) we have

$$|\alpha| \leq 2,$$

i.e.,

$$|(1 - S(\eta))(1 - \eta)| \leq 2. \quad (37)$$

So we choose

$$S(\eta) = \frac{|\eta| - 1}{|\eta| + 1}. \quad (38)$$

It should be pointed out that, besides the lattice Boltzmann equation, the MWB scheme works also for simulating hydrodynamic equations.

4. Combined scheme for the LB evolution

By composing the solutions of the three subequations in Eq.(17), we get the combined scheme for the LB evolution,

$$\begin{aligned} f_{ki}^{t+\Delta t} &= \exp(-\frac{\Delta t}{\tau})[f_{ki}^t - f_{ki}^{eq} + f_{ki}^{eq} \exp(\frac{\Delta t}{\tau})] \\ &- [C_r + \frac{1}{2}C_r(1 - |C_r|)(1 - S(\eta_r))(1 - \eta_r)]\delta_r \\ &- [C_\theta + \frac{1}{2}C_\theta(1 - |C_\theta|)(1 - S(\eta_\theta))(1 - \eta_\theta)]\delta_\theta \end{aligned} \quad (39)$$

where

$$C_r = v_{kir} \frac{\Delta t}{\Delta r}, \quad C_\theta = \frac{1}{r} v_{ki\theta} \frac{\Delta t}{\Delta \theta} \quad (40)$$

$$\begin{aligned} \delta_r &= \begin{cases} f_{ki}(ir, i\theta) - f_{ki}(ir-1, i\theta) & \text{if } v_{kir} \geq 0 \\ f_{ki}(ir+1, i\theta) - f_{ki}(ir, i\theta) & \text{if } v_{kir} < 0 \end{cases} \\ \delta_\theta &= \begin{cases} f_{ki}(ir, i\theta) - f_{ki}(ir, i\theta-1) & \text{if } v_{ki\theta} \geq 0 \\ f_{ki}(ir, i\theta+1) - f_{ki}(ir, i\theta) & \text{if } v_{ki\theta} < 0 \end{cases} \end{aligned} \quad (41)$$

$$\begin{aligned} \eta_r &= \begin{cases} \frac{f_{ki}(ir-1, i\theta) - f_{ki}(ir-2, i\theta)}{f_{ki}(ir, i\theta) - f_{ki}(ir-1, i\theta)} & \text{if } f_{ki}(ir, i\theta) \neq f_{ki}(ir-1, i\theta) \text{ \& } v_{kir} \geq 0 \\ const & \text{if } f_{ki}(ir, i\theta) = f_{ki}(ir-1, i\theta) \text{ \& } v_{kir} \geq 0 \\ \frac{f_{ki}(ir+2, i\theta) - f_{ki}(ir+1, i\theta)}{f_{ki}(ir+1, i\theta) - f_{ki}(ir, i\theta)} & \text{if } f_{ki}(ir+1, i\theta) \neq f_{ki}(ir, i\theta) \text{ \& } v_{kir} < 0 \\ const & \text{if } f_{ki}(ir+1, i\theta) = f_{ki}(ir, i\theta) \text{ \& } v_{kir} < 0 \end{cases} \\ \eta_\theta &= \begin{cases} \frac{f_{ki}(ir, i\theta-1) - f_{ki}(ir, i\theta-2)}{f_{ki}(ir, i\theta) - f_{ki}(ir, i\theta-1)} & \text{if } f_{ki}(ir, i\theta) \neq f_{ki}(ir, i\theta-1) \text{ \& } v_{ki\theta} \geq 0 \\ const & \text{if } f_{ki}(ir, i\theta) = f_{ki}(ir, i\theta-1) \text{ \& } v_{ki\theta} \geq 0 \\ \frac{f_{ki}(ir, i\theta+2) - f_{ki}(ir, i\theta+1)}{f_{ki}(ir, i\theta+1) - f_{ki}(ir, i\theta)} & \text{if } f_{ki}(ir, i\theta+1) \neq f_{ki}(ir, i\theta) \text{ \& } v_{ki\theta} < 0 \\ const & \text{if } f_{ki}(ir, i\theta+1) = f_{ki}(ir, i\theta) \text{ \& } v_{ki\theta} < 0 \end{cases} \end{aligned} \quad (42)$$

Here, ir and $i\theta$ are indexes of the coordinate. To this step, we have got a new conservative monotonous scheme with the second order accuracy.

C. Boundary conditions

The physical domain being considered in this work is an annular region whose radii are $R_2 > R_1 > 0$. When the inner radius $R_1 \rightarrow 0$, the annular region approximates to a circular area. If the annular physical domain is periodic and the period is N_i along the circumferential direction, it can be divided into N_i parts, where N_i is just the total number of the directions of discrete velocity in the DVM. In this case, we can pick out only one part for calculations.

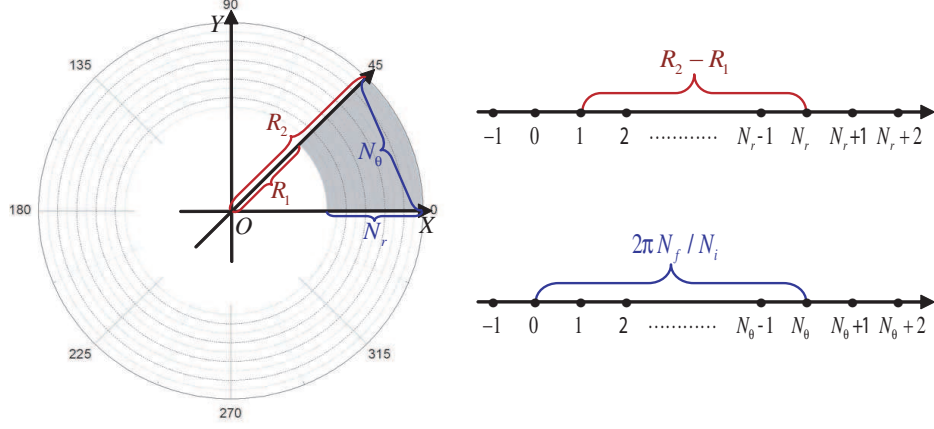


FIG. 2: Sketch for the whole system and the computational domain with lattice nodes.

If the period is N_i/N_f , we can pick out N_f connected parts as computational domain, where N_f is a positive integer. Thus, the computational domain is that with $R_1 \leq r \leq R_2$ and $0 < \theta \leq 2\pi N_f/N_i$. The computational domain has two boundaries in the radial direction and two in the circumferential direction. It is clear that periodic boundary conditions should be applied in the circumferential direction. On the other hand, the inner and outer boundaries in the radial direction should be treated specifically according to the specific situation under consideration. In this work we study the case with $N_i = 8$ and $N_f = 1$. Figure 2 shows a sketch for the computational domain.

1. Radial boundary condition

Assume that the total number of radial nodes is N_r , radial increment is $\Delta r = (R_2 - R_1)/(N_r - 1)$, and the radius $r = R_1 + (ir - 1) \times \Delta r$, where $ir = 1, 2, \dots, N_r$. In the case where the densities can be considered continuous around the boundaries, we can obtain the density values on the ghost nodes ($ir = -1, 0, N_r + 1, N_r + 2$) via linear interpolation scheme,

$$\begin{aligned} \rho(ir, i\theta) &= 2\rho(ir + 1, i\theta) - \rho(ir + 2, i\theta) \quad \text{if } ir < 1 \\ \rho(ir, i\theta) &= 2\rho(ir - 1, i\theta) - \rho(ir - 2, i\theta) \quad \text{if } ir > N_r \end{aligned} \quad (43)$$

or an interpolation scheme with the higher-order accuracy. The temperatures can be calculated in a similar way. However, the determination of flow velocities depends on the specific situation under consideration. The simplest microscopic boundary condition is to assume that at each boundary node the system is in its thermodynamic equilibrium, i.e. $f_{ki} = f_{ki}^{eq}$.

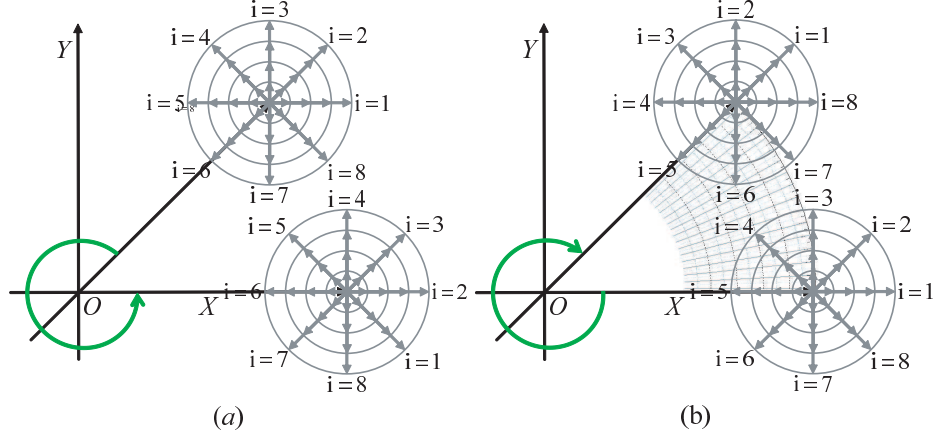


FIG. 3: (a) Rotation from the azimuthal boundary with N_θ to the one with 0. (b) Rotation from the azimuthal boundary with 1 to the one with $N_\theta + 1$.

For the non-equilibrium microscopic boundary condition, the deviation from thermodynamic equilibrium, $f_{ki} - f_{ki}^{eq}$, can be calculated via the interpolation scheme.

2. Azimuthal boundary condition

Similarly, assume that the total number of azimuthal nodes is N_θ , azimuthal increment is $\Delta\theta = 2\pi N_f / (N_i N_\theta)$, and the angle $\theta = i\theta \times \Delta\theta$, where $i\theta = 1, 2, \dots, N_\theta$. The distribution functions on ghost nodes ($i\theta = -1, 0, N_\theta + 1, N_\theta + 2$) are computed in the following way

$$\begin{aligned} f(ir, 0, k, i) &= f(ir, N_\theta, k, i + N_f - N_i) \\ f(ir, -1, k, i) &= f(ir, N_\theta - 1, k, i + N_f - N_i) \end{aligned} \quad (44a)$$

$$\{i + N_f - N_i\} = \begin{cases} i + N_f - N_i & \text{if } i + N_f \geq N_i \\ i + N_f & \text{if } i + N_f < N_i \end{cases},$$

$$\begin{aligned} f(ir, N_\theta + 1, k, i) &= f(ir, 1, k, i + N_i - N_f) \\ f(ir, N_\theta + 2, k, i) &= f(ir, 2, k, i + N_i - N_f) \end{aligned} \quad (44b)$$

$$\{i - N_f + N_i\} = \begin{cases} i - N_f + N_i & \text{if } i - N_f \leq 0 \\ i - N_f & \text{if } i - N_f > 0 \end{cases}.$$

A schematic diagram for the case with $N_i = 8$ and $N_f = 1$ is referred to Fig.3. Figure (a) shows the way in which $f_{ki}(ir, 0)$ is given from $f_{ki}(ir, N_\theta)$ via rotation. Figure (b) shows the relation between $f_{ki}(ir, N_\theta + 1)$ and $f_{ki}(ir, 1)$ via rotation.

III. VALIDATION AND VERIFICATION

A. Performance on rotational slip flow

We first consider the motion of a fluid between two coaxial cylinders, with radii R_1 and R_2 , rotating about their axis with angular velocities ω_1 and ω_2 . It should be pointed out that, the compressibility of the fluid is proportional to the Mach number squared. Our PCLB model is for compressible fluid and physically consistent with this behavior. In this test the Mach number is small, so we roughly consider the system as incompressible. Due to the rotational symmetry, we have $u_r = 0$, $u_\theta = u_\theta(r)$, $P = P(r)$. For simplicity, we rewrite u_θ as u in this test. The Navier-Stokes equation for incompressible flow in cylindrical polar coordinates gives the following two equations:

$$\frac{\partial P}{\partial r} - \rho u^2/r = 0, \quad (45a)$$

$$\mu \left(\frac{\partial^2 u}{\partial r^2} + \frac{1}{r} \frac{\partial u}{\partial r} - \frac{u}{r^2} \right) = 0. \quad (45b)$$

The second has the following solution,

$$u = A + \frac{B}{r} \quad (46)$$

where the constants A and B are found from the boundary conditions,

$$\begin{cases} u = R_1 \omega_1 & \text{for } r = R_1 \\ u = R_2 \omega_2 & \text{for } r = R_2 \end{cases}. \quad (47)$$

As a result, we get the velocity distribution to be

$$u = \frac{\omega_2 R_2^2 - \omega_1 R_1^2}{R_2^2 - R_1^2} r + \frac{R_1^2 R_2^2 (\omega_1 - \omega_2)}{R_2^2 - R_1^2} \frac{1}{r} \quad (48)$$

which is a non-slip Navier-Stokes solution and is independent of the viscosity μ .

Initially, the system is in its thermodynamic equilibrium with $\rho = 1.0$, $T = 1$ and $u_r = 0$, $u_\theta = 0$. The other parameters are given as $R_1 = 1$, $R_2 = 2$, $\omega_1 = -0.1$, $\omega_2 = 0.1$, $\Delta t = 10^{-3}$, $N_r \times N_\theta = 100 \times 20$. Figure 4 shows the comparison of the LB results and the Analytic Solution(AS) for the final steady state, where the values of relaxation time τ are 0.2, 0.1, 0.05, and 0.01, respectively. We can find that the simulation results have a satisfying agreement with AS. The slight mismatch is due to the weak compressibility of the fluid which is ignored in the analytical solution.

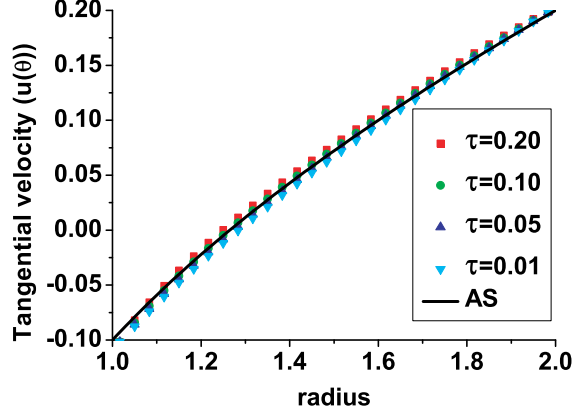


FIG. 4: Comparison of LB results and analytical solution for the steady rotational velocity u_θ under various values of τ .

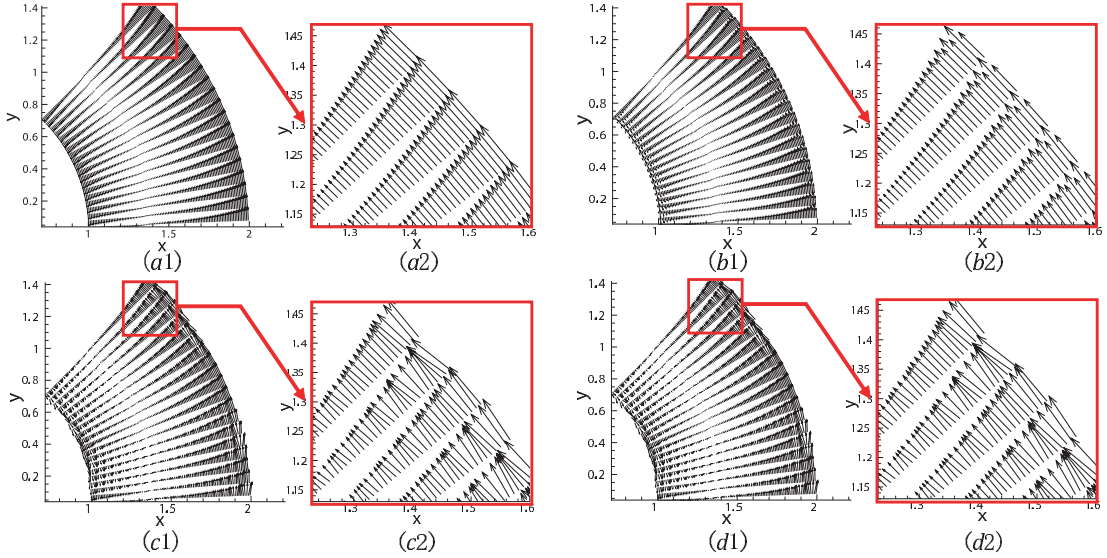


FIG. 5: The plane description of velocity field about the rotational slip flow at time $t = 0.6$: (a) the MWB scheme; (b) Lax-Wendroff scheme; (c) the second order upwind scheme; (d) Warming-Beam scheme.

To compare our MBW scheme with other FD schemes for the convection term, we show, in Fig.5, the simulation results of velocity field at time $t = 0.6$. The FD schemes used in Figs.(a1)-(d1) are our MWB scheme, the Lax-Wendroff scheme, the second order upwind scheme, and the original Warming-Beam scheme, respectively. Figures (a1)-(d1) show the global velocity fields in the computational domain. What Figs.(a2)-(d2) show are the enlargements of the portions in the corresponding squares in Figs.(a1)-(d1). From Fig.5(b2)

it is clear that the Lax-Wendroff scheme brings artificial oscillations in the tangential component of flow velocities near the inner and outer boundaries. Figures 5(c2) and 5(d2) show that both the second order upwind and the original Warming-Beam schemes bring artificial oscillations in the radial component of flow velocities in the whole computational domain. The simulation result based on our new scheme has a satisfying agreement with theoretical analysis.

B. Performance on discontinuity

To check the performance of our new scheme on system with discontinuity, we consider a shock wave propagating outward in an annular system with radii R_1 and R_2 . The physical quantities in shocked region and pre-shocked region satisfy the following Hugoniot relations,

$$\begin{cases} \rho(u - D) = \rho_0(u_0 - D) \\ P - P_0 = \rho_0(D - u_0)(u - u_0) \\ E - E_0 = \frac{1}{2}(P + P_0)\left(\frac{1}{\rho_0} - \frac{1}{\rho}\right) \end{cases} \quad (49)$$

where D is the velocity of shock wave. Due to the rotational symmetry, u means u_r in the above equations.

The initial physical field is below

$$\begin{cases} (\rho, u_r, u_\theta, P)_{inner} = (1.58824, 0.785674, 0, 2.66667) , & R_1 \leq r < R_S \\ (\rho, u_r, u_\theta, P)_{outer} = (1, 0, 0, 1) , & R_S \leq r < R_2 \end{cases}$$

where R_S is the position of shock front. We choose $R_1 = 2000$, $R_2 = 2025$, $R_S = 2001$, $D = 2.12132$, $\tau = 10^{-5}$, $\Delta t = 10^{-5}$, $N_r \times N_\theta = 250 \times 3$.

Figure 6 shows the simulation results of pressure P , density ρ , temperature T and velocity u_r along the radius at time $t = 8$ using various schemes. From left to right, the four columns correspond to our MWB scheme, the Lax-Wendroff scheme, the second order upwind scheme, and the original Warming-Beam scheme, respectively. It is clear from the second column that the simulated physical fields from the Lax-Wendroff scheme have strong unphysical oscillations in the shocked region. The third column shows that the second order upwind scheme results in unphysical “overshoot” phenomena in the pressure, density, temperature and flow velocity at the shock front. The fourth column shows that the original Warming-Beam has the same drawback as that of the second order upwind scheme. Contrast to the

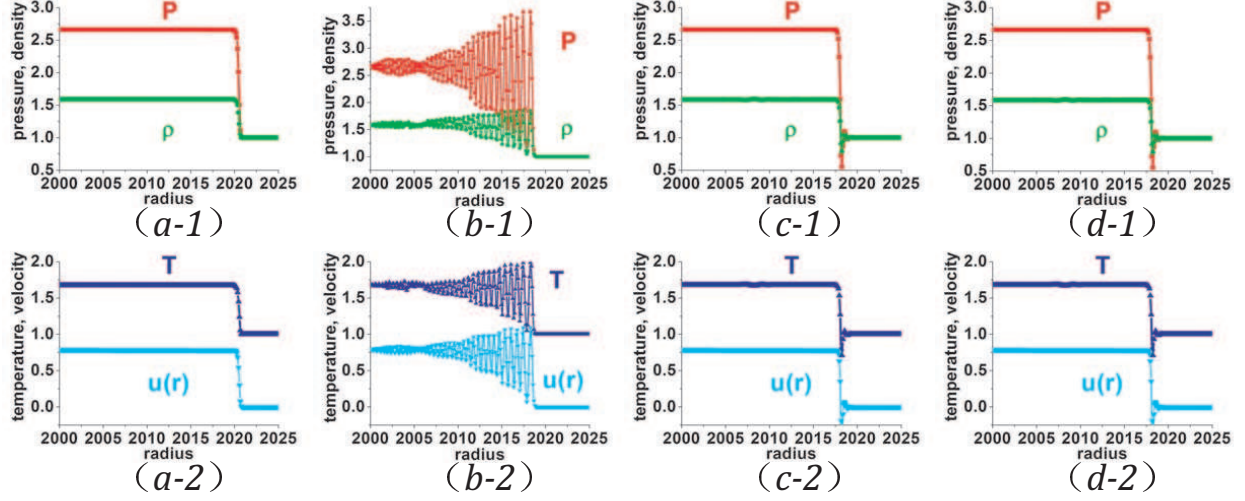


FIG. 6: The distributions of pressure P , density ρ , temperature T and velocity u_r along the radius using various schemes. From left to right, the four columns correspond to the MWB scheme, Lax-Wendroff scheme, second order up wind scheme and Warming-Beam scheme.

other three columns, the first column shows that the simulation results from our MWB are much more accurate and physically reasonable.

C. Simulation study on Richtmyer-Meshkov instability

The Richtmyer-Meshkov(RM) instability takes place when a shock wave travels across an interface separating two kinds of fluids. For the one-dimensional system with plane shock wave, several models have been proposed to describe the increase of the amplitude A . Roughly speaking, the increase rate of A first shows a linear relationship with itself, i.e., $dA/dt = cA$, where c is the increasing coefficient. In other words, the amplitude A increases exponentially with time according to the relation, $A = A_0 \exp(ct)$. When the time t is very small, $\exp(ct) = 1 + ct$, $A = A_0 + A_0 ct$. It is clear that, at the very beginning, the amplitude A linearly increases with time t . In the later time, the increasing coefficient c itself is no longer a constant any more. Therefore, the later stage is generally referred to as the nonlinear increasing stage.

In 1960 Richtmyer [47] modified the linear theory of Taylor for Rayleigh-Taylor instability and proposed an impulsive model in the case of a reflected shock wave. The growth rate

reads,

$$\frac{dA}{dt} = k\Delta u A_t A_1, \quad A_1 = A_0 \left(1 - \frac{\Delta u}{D}\right)$$

where $k = 2\pi/\lambda$ is the wave number, Δu is the velocity change of the interface when shock passes, A_t represents the post-shock Atwood number, A_1 is the post-shock amplitude, A_0 is the initial amplitude. $Cmpr = 1 - \Delta u/D$ is defined as compression ratio. In 1969 Meshkov [48] measured growth rate and found that it is only about one half of that predicted by the impulsive model. In 1992 Benjamin [49] got similar experiment results. In 1997 Zhang and Sohn [50] developed the following model

$$\frac{dA}{dt} = \frac{v_0}{1 + k^2 v_0 A_1 t + \max[0, (kA_1)^2 - (A_1)^2 + 0.5](kv_0 t)^2}$$

where $v_0 = k\Delta u A_1 A_1$. This model is the growth rate of the interface amplitude from early to late times in the case of transition from light medium to heavy one.

In an annular system with radii $R_1 = 1.0$ and $R_2 = 2.0$, we study the RM instability in the following two cases: shocking from light to heavy media and shocking from heavy to light media. We consider the case where an initial sinusoidal perturbation, $r = R + A_0 \times \cos(kR\theta)$, is applied to the density field, where R is the average position of the interface between the two media. Even though the system considered here shows two-dimensional effects, for the case where the perturbation wave length is small and the inner radius is large enough, the above theory for one-dimensional system with plane shock wave still works approximately.

1. Shocking from light to heavy media

We consider the case where a shock wave travels outward from the light medium to the heavy one with the velocity $D = 2$. The initial physical field is given as below

$$\begin{cases} (\rho, u_r, u_\theta, P)_{inner} &= (1.5, 0.6666667, 0, 2.333333) \\ (\rho, u_r, u_\theta, P)_{middle} &= (1, 1, 0, 1) \\ (\rho, u_r, u_\theta, P)_{outer} &= (3, 1, 0, 1) \end{cases}$$

where the subscripts *inner* and *middle* indicate shocked and pre-shocked regions of light medium, *outer* represents outer region where the heavy medium locates. The numerical values between the shocked and pre-shocked regions satisfy with the Hugoniot relations. We choose $A = 0.02$, $R = 1.2$, $k = 20$, $\tau = \Delta t = 10^{-5}$, $N_r \times N_\theta = 1000 \times 450$.

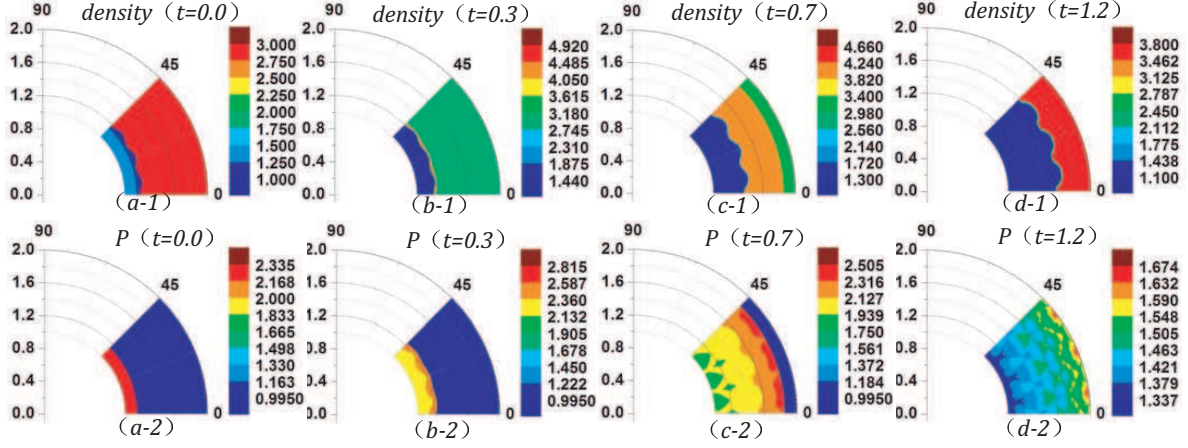


FIG. 7: Snapshots of RM instability for the case where the shock wave travels outwards from the light to heavy media. The density and pressure fields at the times, $t = 0$, $t = 0.05$, $t = 0.5$, $t = 1.2$, are shown from left to right, respectively.

Figure 7 shows the snapshots of the density and pressure fields. The first row is for the density fields. The second is for the pressure fields. From left to right, the four columns are for the times, $t = 0$, $t = 0.05$, $t = 0.5$, $t = 1.2$, respectively. When the shock wave passes the interface, the perturbation amplitude A in the density field first decreases significantly due to compression of the shock wave, see Figs.(a-1)-(b-1), then it begins to increase under the pressure gradient, see Figs.(b-1)-(d-1), where asymmetric structures at the two sides of the interface eventually result in the occurrence of the bubbles in the light medium and spikes in the heavy medium. The corresponding pressure fields shown in Figs. (a-2)-(d-2) present complementary information for understanding the evolution of the density field. It should be pointed out that the misalignment of pressure and density gradients promotes deformation.

In order to draw some quantitatively information to compare with the above theory, we show, from left to right in Fig.8, the amplitude, growth rate, average radial position and velocity of perturbation interface with time, where $t = 0$ is defined as the time when the shock meets with the perturbation interface, and the amplitude is defined as half of the maximum distance from the crest to trough. From Fig.(a) we can observe clearly the compression and recovery of the perturbation amplitude. In the compressure process the amplitude drops rapidly, it decreases to the minimum $A_{comp} = 0.0143$ at the time $t_{comp} = 0.03$ and recovers to its initial value at the time $t_{reco} = 0.13$. For the convenience of analysis, a vertical line is plotted to guide the eyes in each of the Figs.(a)-(d) to indicate the time,

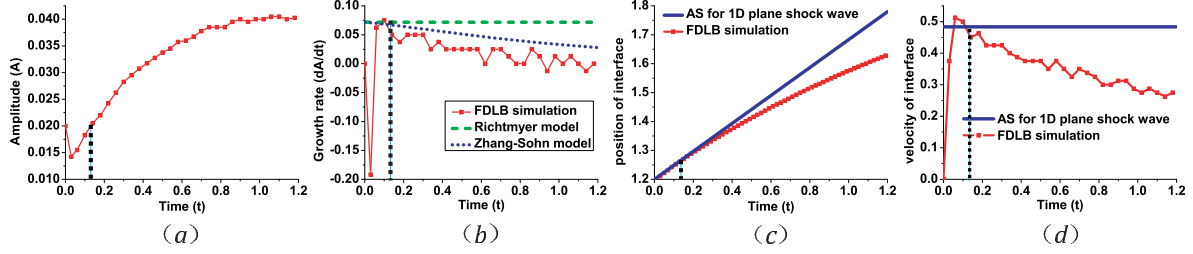


FIG. 8: Descriptions of RM instability for the case where shock wave travels outwards from light medium to heavy one. (a) Amplitude simulated by our model. (b) Growth rate of different models. (c) Averaged radial position. (d) Velocity of perturbed interface. A vertical line is shown in each plot to guide the eyes for the time when the interface width recovers to its original value.

t_{rec} , when the interface width recovers its original value. The evolution process of the perturbation amplitude before the time t_{rec} is referred to as the initial compressure and recovery stage and after that is referred to as the increasing stage. From the minimum value in Fig.(a), we get the compression ratio $Cmpr = 0.0143/0.02 = 0.715$. However, the theoretical solution based on the initial conditions is $Cmpr = 0.758$. The deviation of the simulation result from the theoretical one is about 6%. In Fig.(b) the simulated growth rate of the perturbation amplitude A qualitatively agrees well with those theoretical models in the recover stage. It should be pointed out that, after taking into account the two-dimensional effects existing in this test system but are ignored by the theory, the simulation result shows a satisfying agreement with the theory. In Figs.(c) and (d) we compare the position and velocity of interface, respectively, for two cases. The first case is the simple one-dimensional problem where the plane shock wave passes the plane interface of two fluids. The second case is for the situation under consideration. We can find that the velocity of perturbation interface is slower than that for the case with plane shock wave. Physically, in the first case, the shock wave does not result in transverse flow velocity, the interface propagates in one direction at a constant velocity; while in the second case, two reasons result in the decreasing of the propagation velocity of the interface. On the one hand, the RM instability results in vortexes of flows. The transverse motion distracts part of the kinetic energy. Consequently, the propagation velocity in the original direction becomes slower. On the other hand, the geometrical structure of the setup leads to a slower propagation velocity. During the propagation process, the radius where the interface locates becomes larger, the

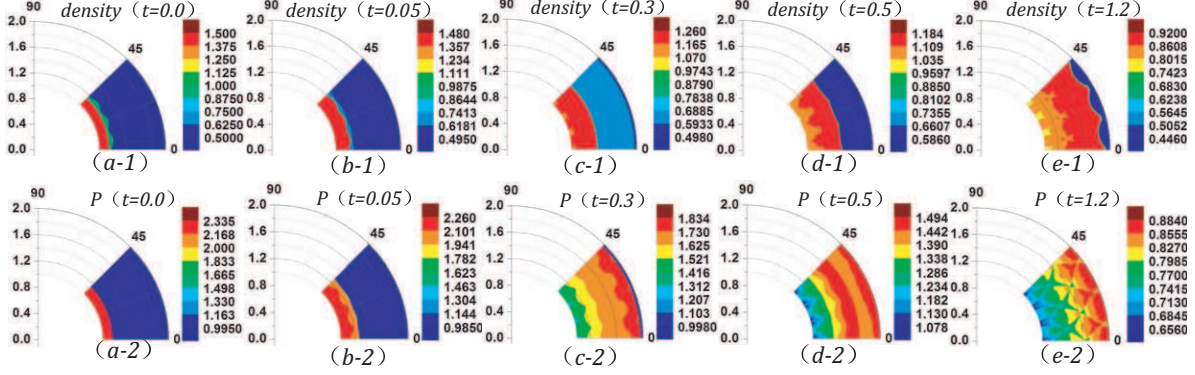


FIG. 9: Snapshots of RM instability for the case where the shock wave travels outwards from the heavy to light media. The density and pressure fields at the times, $t = 0, 0.05, 0.5$, and 1.2 , are shown from left to right, respectively.

area of the interface becomes larger. The distraction of kinetic energy makes slower the propagation velocity in the radial direction.

2. Shocking from heavy to light media

In the subsequent simulation, we choose $\rho_{inner} = 1$, $\rho_{outer} = 0.5$, and other parameters are the same as those in the above simulation.

We show the simulation results for density and pressure fields at times $t = 0.0, 0.05, 0.3, 0.5$, and 1.2 in Fig.9, where the interface reversal phenomenon is obviously observed. Simulation results show the following physical procedure: when the shock wave passes the interface, a rarefaction wave reflected inward and a transmission wave outward are generated. Near the crest, the pressure of heavy medium is smaller than that of the light medium. Driven by the pressure gradient, the perturbation amplitude decreases with the outward motion of the interface. Then, the peak and valley of initial interface invert, the heavy and light fluids gradually penetrate into each other as time goes on, the light fluid “falls” to form a bubble and the heavy fluid “rises” to generate a spike.

We show the change of perturbation interface with time in Fig.10. Figure (a) shows the simulated amplitude. Figure (b) shows the growth rate, where the line with scatters is for the LB result, the dashed line shows result from the Richtmyer model, and the dotted line is for the absolute value of result from the Richtmyer model. Figures (c)-(d) show the average

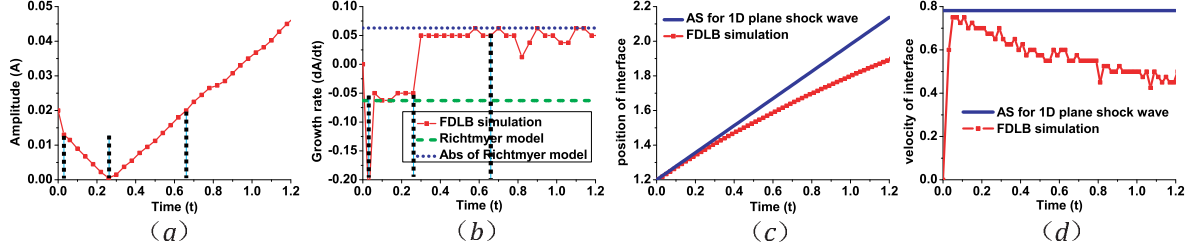


FIG. 10: Descriptions of RM instability for the case where shock wave travels outwards from heavy medium to light one. (a) Amplitude simulated by our model. (b) Growth rates from LB simulation, from the original Richtmyer model and from the absolute value of Richtmyer model. (c) Averaged radial position. (d) Velocity of perturbed interface. Three vertical lines are shown in each plot to guide the eyes for the compression, reversal, recovery and increasing stages.

radial position and velocity of perturbed interface. Three vertical lines are shown in Figs.(a) and (b) to divide the evolution progress into four stages, i.e., the stages of compression, reversal, recovery and increasing. The first guideline corresponds to the time, $t_{comp} = 0.03$, when the amplitude is rapidly compressed to $A_{comp} = 0.013$. The second one is for the time, $t_{zero} = 0.27$, when the amplitude reaches zero. The last one indicates the time, $t_{reco} = 0.66$, when the amplitude recovers to its initial value, $A_{init} = 0.02$. From Fig.(a) we can get the compression ratio $Cmpr = 0.013/0.02 = 0.65$. As a comparison, the theoretical solution is $Cmpr = 0.61$. From Fig.(b) we can find that, for the evolution process of RM instability, our simulation result is close to that of Richtmyer model. Figures (c) and (d) show the same phenomena as those in Fig.8.

D. Simulation study on Kelvin-Helmholtz instability

To investigate the Kelvin-Helmholtz(KH) instability in annular region with radii $R_1 < R_2$, we set the initial physical field as below,

$$\rho(r) = \frac{\rho_{inner} + \rho_{outer}}{2} - \frac{\rho_{inner} - \rho_{outer}}{2} \tanh\left(\frac{r - R}{D_\rho}\right), \quad (50a)$$

$$\mathbf{u}(r) = \frac{\mathbf{u}_{inner} + \mathbf{u}_{outer}}{2} - \frac{\mathbf{u}_{inner} - \mathbf{u}_{outer}}{2} \tanh\left(\frac{r - R}{D_u}\right), \quad (50b)$$

$$P(r) = P_{inner} = P_{outer}, \quad (50c)$$

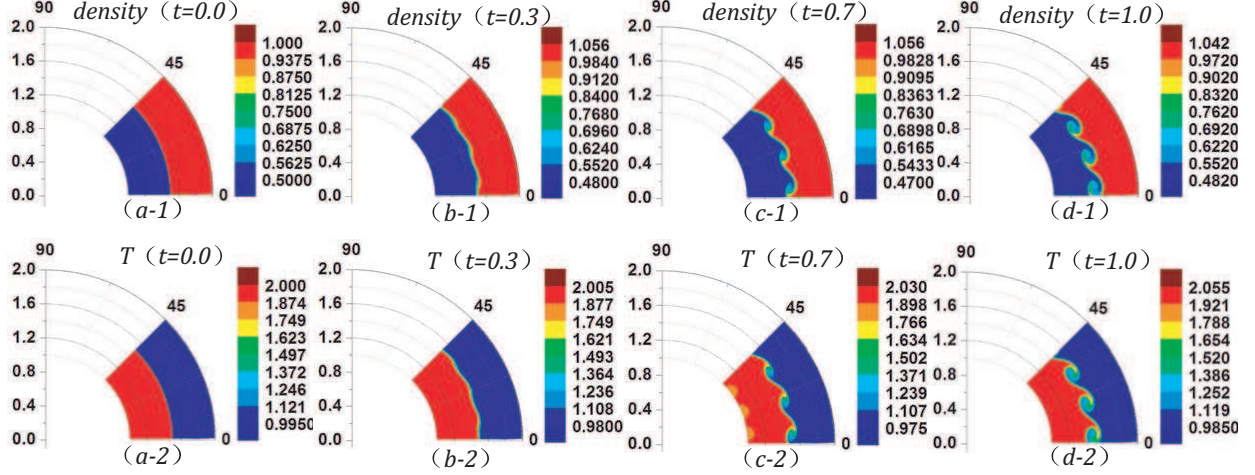


FIG. 11: Snapshots of KH instability for the case $\rho_{inner} < \rho_{outer}$. The four columns are for the density and temperature contours at $t = 0, 0.3, 0.7$, and 1 , respectively.

where D_ρ and D_u are the widths of density and velocity transition layers. ρ_{inner} , \mathbf{u}_{inner} and P_{inner} (ρ_{outer} , \mathbf{u}_{outer} and P_{outer}) are the density, velocity and pressure of fluid near the inner (outer) cylinder, respectively. R is the radial position of interface between two media. In order to trigger the KH rollup, the following perturbation of velocity in the r -direction,

$$u_r \mathbf{e}_r = u_0 \mathbf{e}_r \sin(kR\theta) \exp(-|r - R|), \quad (51)$$

is added to the initial velocity field described by Eq.(50b), where $u_0 = 0.5$ is the amplitude of the perturbation, k is wave number. We study the KH instability in the following two cases: $\rho_{inner} < \rho_{outer}$ and $\rho_{inner} > \rho_{outer}$.

1. Case of $\rho_{inner} < \rho_{outer}$

In the subsequent simulation, we choose $\rho_{inner} = 0.5$, $\rho_{outer} = 1.0$, $\mathbf{u}_{outer} = 0.5\mathbf{e}_\theta$, $\mathbf{u}_{inner} = -0.5\mathbf{e}_\theta$, $D_\rho = D_u = 0.1$, $R_1 = 1$, $R_2 = 2$, $R = 1.5$, $k = 16$, $\tau = \Delta t = 10^{-5}$, $N_r \times N_\theta = 200 \times 90$. We plot the density and temperature contours at the times, $t = 0, 0.3, 0.7$, and 1 , respectively in Fig.11. Figure (a) shows the initial state, where the interface starts to roll up gradually under the influence of the disturbance in Eq.(51). In Figs.(b)-(d) we can observe that the deformation of interface caused by the KH instability become more significant with time.

Let's study the spatial distribution of density and pressure at time $t = 1$ in Fig.12. Figures

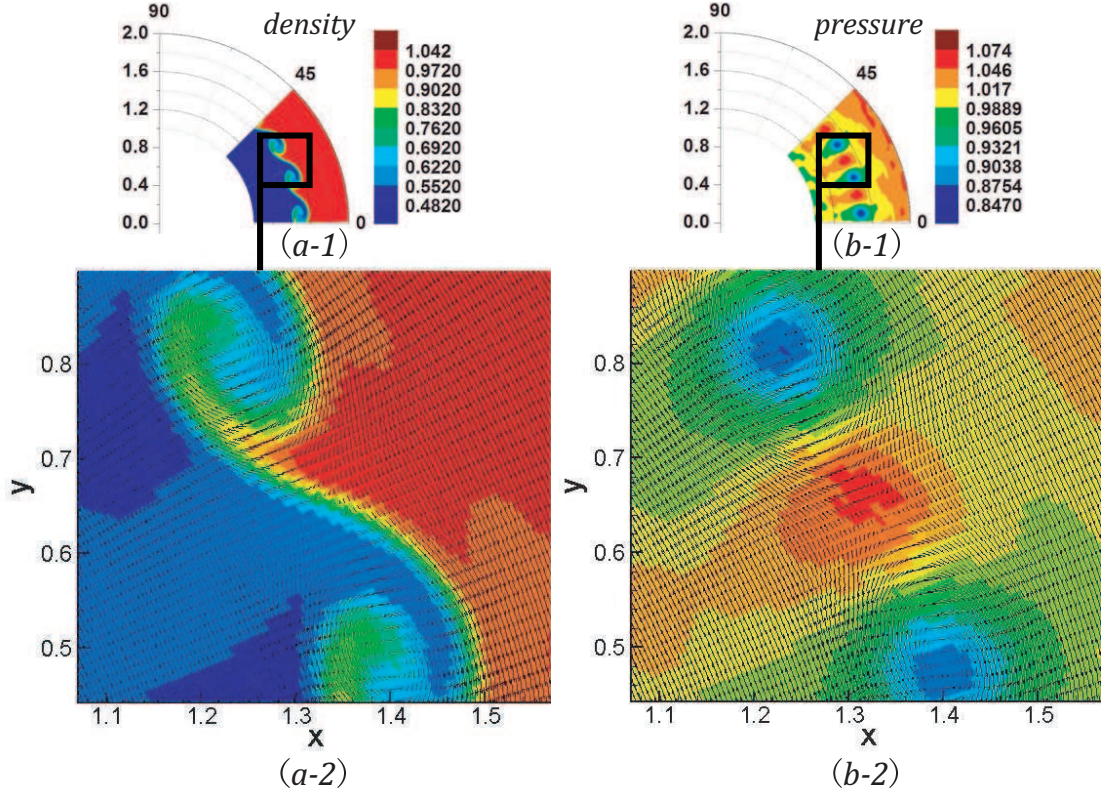


FIG. 12: Snapshots at time $t = 1$ for the case $\rho_{inner} < \rho_{outer}$. (a-1) and (b-1) show the contours of density and pressure. (a-2) shows more clearly the contour of density with velocity field in the region labeled by the square in (a-1). (b-2) shows more clearly the contour of pressure with velocity field in the region labeled by the square in (b-1).

(a-1) and (b-1) show the contours of density and pressure. Figure (a-2) shows more clearly the contour of density with velocity field in the region labeled by the square in Fig. (a-1). Figure (b-2) shows more clearly the contour of pressure with velocity field in the region labeled by the square in Fig. (b-1). From the velocity field in Fig. (a-2) we conceive that the KH instability would continue to develop and promote the intermixing and penetrating of the two fluids at the interface. It's clear to find in Fig. (b-2) that the pressure is in its minimum at the center of the vortex, and it is the pressure gradient that offers the centripetal force required for rotating.

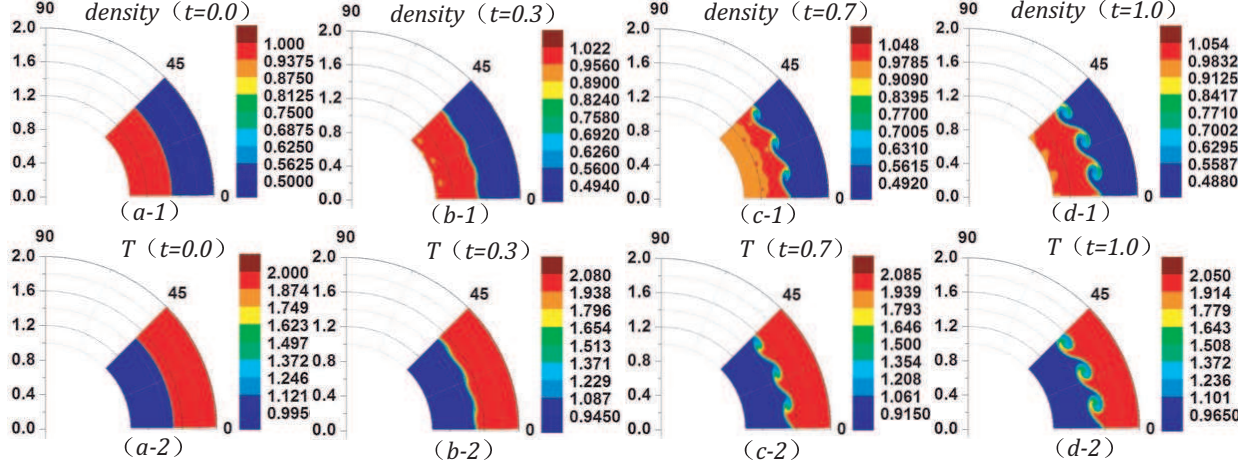


FIG. 13: Snapshots of KH instability for the case $\rho_{inner} > \rho_{outer}$. The four columns are for the density and temperature contours at $t = 0, 0.3, 0.7$, and 1 , respectively.

2. Case of $\rho_{inner} > \rho_{outer}$

In the subsequent simulation, $\rho_{inner} = 1.0$, $\rho_{outer} = 0.5$, other parameters are the same as those in the case $\rho_{inner} < \rho_{outer}$. We show the density and density contours at $t = 0, 0.3, 0.7$, and 1 , respectively in Fig.13, where the physical mechanism is similar to that in Fig.11. From Figs.11 and 13 we find that the structures within the heavy medium are relatively sharp, likely “finger”; while the ones within the light medium are relatively smooth, likely “bubble”.

Figure 14 shows the spatial distributions of density, pressure and velocity at $t = 1$. From Figs.12 and 14 we find that the pressure is in its minimum at the vortex center and is in its maximum at the junction of vortices.

It should be pointed out that, in the case of $\rho_{inner} > \rho_{outer}$ above, besides the KH instability, the Rayleigh-Taylor (RT) instability generally plays also a role in the rotating procedure of material. Because inertia presents an acceleration pointing to the light medium from the heavy one. But since the observation time is short, what we observe is mainly the result of the KH instability.

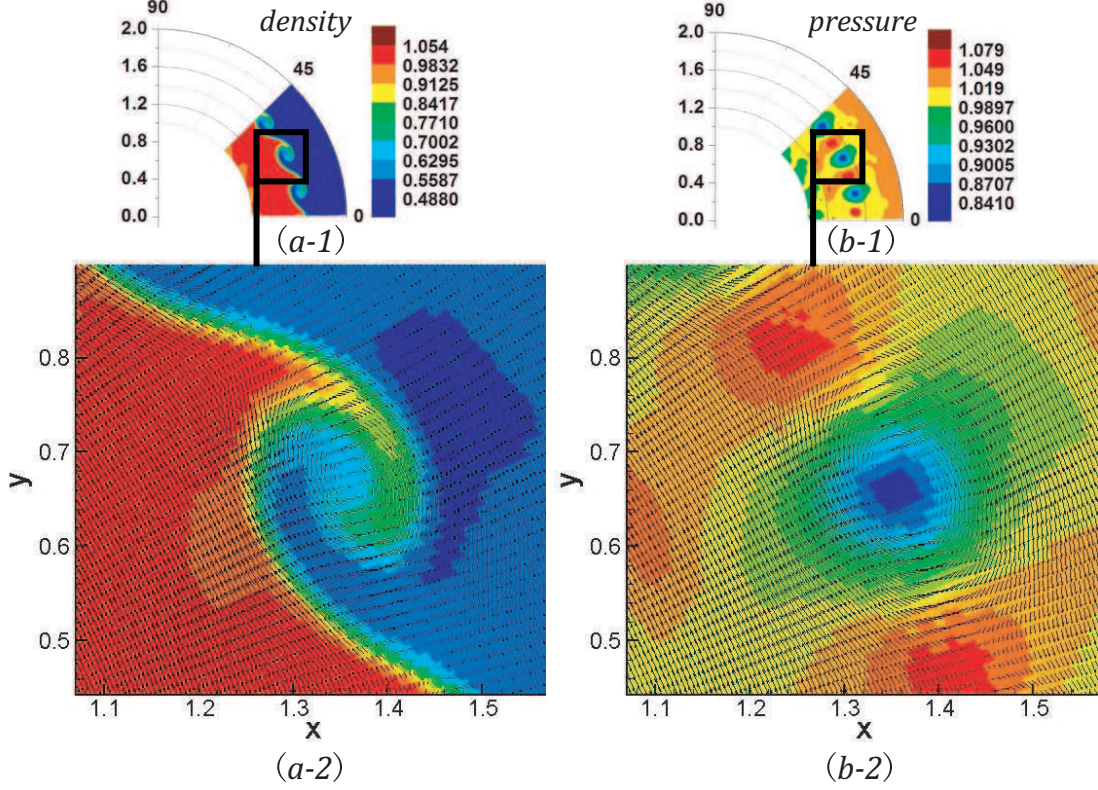


FIG. 14: Snapshots at time $t = 1$ for the case $\rho_{inner} > \rho_{outer}$. (a-1) and (b-1) show the contours of density and pressure. (a-2) shows more clearly the contour of density with velocity field in the region labeled by the square in (a-1). (b-2) shows more clearly the contour of pressure with velocity field in the region labeled by the square in (b-1).

IV. NON-EQUILIBRIUM CHARACTERISTICS IN TWO SPECIFIC CASES

To show the merit of the LB model over traditional ones, in this section we study the non-equilibrium characteristics in two specific cases. Among the seven moment relations, Eqs.(3)-(9), required by our model, only for the first three the equilibrium distribution function f_{ki}^{eq} can be replaced by the distribution function f_{ki} . If we replace f_{ki}^{eq} by f_{ki} in the left hand side of any one of Eqs.(6)-(9), the left and right hand sides of Eqs.(6)-(9) will no longer be in balance. This mismatch measures the departure of the system from local thermodynamic equilibrium.

We define two kinds of space-time dependent fields, moments \mathbf{M}_m and central moments

\mathbf{M}_m^* , as given below:

$$\left\{ \begin{array}{l} \mathbf{M}_2(f_{ki}) = \sum_{ki} f_{ki} \mathbf{v}_{ki} \mathbf{v}_{ki} \\ \mathbf{M}_3(f_{ki}) = \sum_{ki} f_{ki} \mathbf{v}_{ki} \mathbf{v}_{ki} \mathbf{v}_{ki} \\ \mathbf{M}_{3,1}(f_{ki}) = \sum_{ki} \frac{1}{2} f_{ki} \mathbf{v}_{ki} \cdot \mathbf{v}_{ki} \mathbf{v}_{ki} \\ \mathbf{M}_{4,2}(f_{ki}) = \sum_{ki} \frac{1}{2} f_{ki} \mathbf{v}_{ki} \cdot \mathbf{v}_{ki} \mathbf{v}_{ki} \mathbf{v}_{ki} \end{array} \right. \quad (52)$$

$$\left\{ \begin{array}{l} \mathbf{M}_2^*(f_{ki}) = \sum_{ki} f_{ki} (\mathbf{v}_{ki} - \mathbf{u})(\mathbf{v}_{ki} - \mathbf{u}) \\ \mathbf{M}_3^*(f_{ki}) = \sum_{ki} f_{ki} (\mathbf{v}_{ki} - \mathbf{u})(\mathbf{v}_{ki} - \mathbf{u})(\mathbf{v}_{ki} - \mathbf{u}) \\ \mathbf{M}_{3,1}^*(f_{ki}) = \sum_{ki} \frac{1}{2} f_{ki} (\mathbf{v}_{ki} - \mathbf{u}) \cdot (\mathbf{v}_{ki} - \mathbf{u})(\mathbf{v}_{ki} - \mathbf{u}) \\ \mathbf{M}_{4,2}^*(f_{ki}) = \sum_{ki} \frac{1}{2} f_{ki} (\mathbf{v}_{ki} - \mathbf{u}) \cdot (\mathbf{v}_{ki} - \mathbf{u})(\mathbf{v}_{ki} - \mathbf{u})(\mathbf{v}_{ki} - \mathbf{u}) \end{array} \right. \quad (53)$$

where the subscript “3,1” means that the 3rd-order tensor is contracted to a 1st-order tensor and the similar for “4,2”. The moment $\mathbf{M}_{3,1}(= M_{3,1,\alpha} \mathbf{e}_\alpha)$ is a vector. It has two components, $M_{3,1,r}$ and $M_{3,1,\theta}$. The moment $\mathbf{M}_2(= M_{2,\alpha\beta} \mathbf{e}_\alpha \mathbf{e}_\beta)$ is a second-order tensor with four components. Among the four components, only three, $M_{2,rr}$, $M_{2,r\theta}$ and $M_{2,\theta\theta}$, are independent. The case for the moment $\mathbf{M}_{4,2}(= M_{4,2,\alpha\beta} \mathbf{e}_\alpha \mathbf{e}_\beta)$ is similar. The moment $\mathbf{M}_3(= M_{3,\alpha\beta\gamma} \mathbf{e}_\alpha \mathbf{e}_\beta \mathbf{e}_\gamma)$ is a third-order tensor with eight components. Among the eight components, only four, $M_{3,rrr}$, $M_{3,rr\theta}$, $M_{3,r\theta\theta}$ and $M_{3,\theta\theta\theta}$, are independent. The central moments \mathbf{M}_m^* is mathematically similar to \mathbf{M}_m .

The central moment \mathbf{M}_2^* associates with the variance of the distribution function. Its trace associates with the temperature and its off-diagonal components associate with the shear effects. The former is a conserved quantity. When the system is not in its thermodynamic equilibrium state, the latter may not be zero. The moment $\mathbf{M}_{3,1}$ associates with the heat flux. For the equilibrium state, it describes convection of energy. For the non-equilibrium state, besides the energy convection, it includes also the thermodiffusion. For the central moment $\mathbf{M}_{3,1}^*$, a breaking of the $f(\mathbf{v}) = f(-\mathbf{v})$ symmetry allows to eventually transport heat without necessarily carrying a net flow. The third-order central moment \mathbf{M}_3^* may not be zero, while the first-order central moment $\mathbf{M}_1^* = \sum_{ki} f_{ki} (\mathbf{v}_{ki} - \mathbf{u})$ must be zero. In probability theory, for the one-dimensional distribution function $f(v)$, the central moment $M_3^* = \int dv f(v) (v - u)^3$ is called “skewness”. The fourth-order central moment $M_4^* = \int dv f(v) (v - u)^4$ describes the “flatness” of the distribution and is also called “kurtosis”. For a Gaussian distribution function, $f(v) = 1/\sqrt{2\pi} \exp[-(v - u)^2/2]$, $M_4^* = 3$. For the case with $M_4^* > 3$ and $M_2^* = 1$, the distribution is sharper than the Gaussian at the central position.

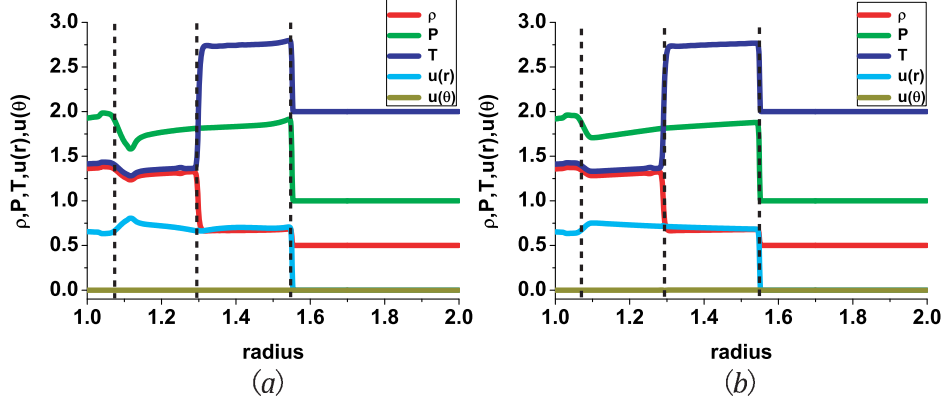


FIG. 15: Profiles of physical quantities (ρ , P , T , u_r , u_θ) in the process of shock wave passing outwards from the heavy medium to the light one. The time $t = 0.15$. (a) Without initial perturbation at the interface. (b) With initial sinusoidal perturbation at the interface. Three lines are shown to guide the eyes for the interfaces.

By Galilean invariance, it is clear that the moment \mathbf{M}_m contains the information of the macroscopic flow velocity \mathbf{u} , while the moment \mathbf{M}_m^* is only the manifestation of the thermo-fluctuations of molecules relative to the macroscopic flow velocity \mathbf{u} .

The manifestations of deviating from thermodynamic equilibrium from the two kinds of moments are as below:

$$\Delta_m = \mathbf{M}_m(f_{ki}) - \mathbf{M}_m(f_{ki}^{eq}) = \mathbf{M}_m(f_{ki} - f_{ki}^{eq}) \quad (54)$$

$$\Delta_m^* = \mathbf{M}_m^*(f_{ki}) - \mathbf{M}_m^*(f_{ki}^{eq}) = \mathbf{M}_m^*(f_{ki} - f_{ki}^{eq}) \quad (55)$$

Similarly, Δ_m contains the information of the macroscopic flow velocity \mathbf{u} , while Δ_m^* does not.

A. Simulation results and analysis

Now, we study the dynamic procedure where a shock wave propagates outwards from the heavy material to the light one. As the first step, we study the simplest situation where the incident shock wave is perpendicular to the unperturbed circular interface. In the second case, the interface is perturbed sinusoidally, and consequently the RM instability will occur. We choose such a time, $t = 0.15$, when the system shows three different interfaces. From left to right, the first is for the rarefaction wave, the second is for the two materials under

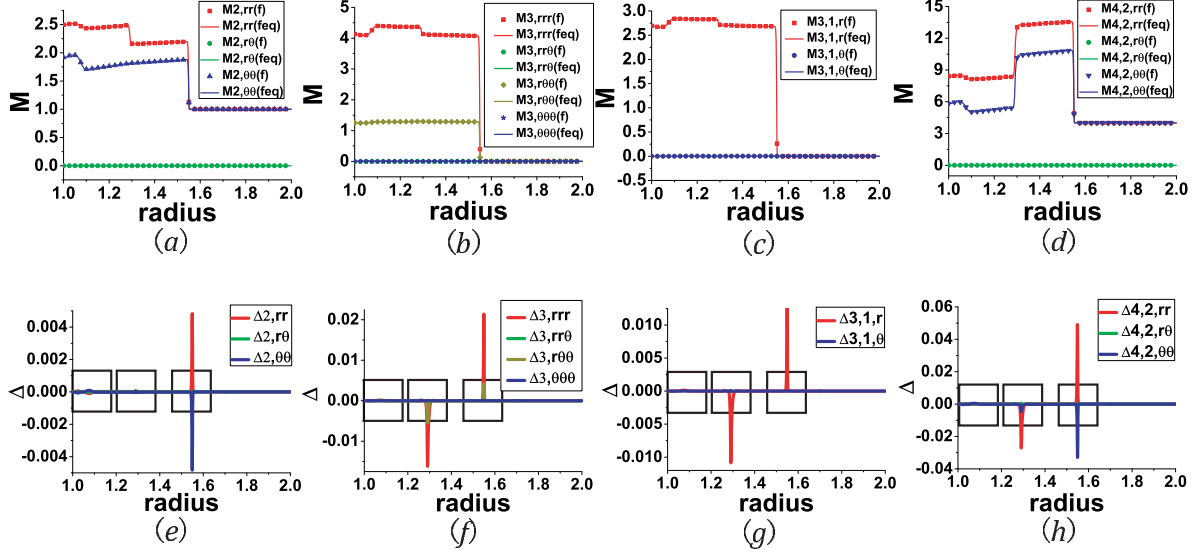


FIG. 16: Moments and their corresponding non-equilibrium manifestations for the case without perturbation at the material interface. The time $t = 0.15$. Figures (a)-(d) are for \mathbf{M}_2 , \mathbf{M}_3 , $\mathbf{M}_{3,1}$, $\mathbf{M}_{4,2}$, respectively. The symbols are for moments from f_{ki} and the solid lines are for moments from f_{ki}^{eq} . Figures (e)-(h) are for deviations Δ_2 , Δ_3 , $\Delta_{3,1}$, $\Delta_{4,2}$, respectively. Only independent components of \mathbf{M}_m and Δ_m are shown. The specific correspondences are referred to the legends. Three squares are shown to guide the eyes for the interfaces.

consideration, the third is for the shock wave.

Figure 15 shows the profiles of physical quantities (ρ , P , T , u_r , u_θ) along the radius with the azimuthal angle $\theta = \pi/6$. Figure (a) corresponds to the case without initial perturbation at interface. Figure (b) is for the case with initial sinusoidal perturbation at the interface. Three lines are shown to guide the eyes for the interfaces. From Fig.15 we can find that physical quantities change significantly at the three interfaces. For the case without perturbation in the material interface, we show the results of \mathbf{M}_m and Δ_m in Fig.16. All independent components of \mathbf{M}_m , and Δ_m are shown. The specific correspondences are referred to the legends. The 12 plots in Fig.17 are the enlargements of the 12 portions labeled by the 12 squares in Fig.16. Figures 17(a)-(d) correspond to the portions labeled by the first squares in Figs.16(e)-(h), respectively. Figures 17(e)-(h) correspond to the portions labeled by the second squares in Figs.16(e)-(h), respectively. Figures 17(i)-(l) correspond to the portions labeled by the third squares in Figs.16(e)-(h), respectively. The results of \mathbf{M}_m^* and Δ_m^* are shown in Fig.18. The 12 plots in Fig.19 are the enlargements of the 12

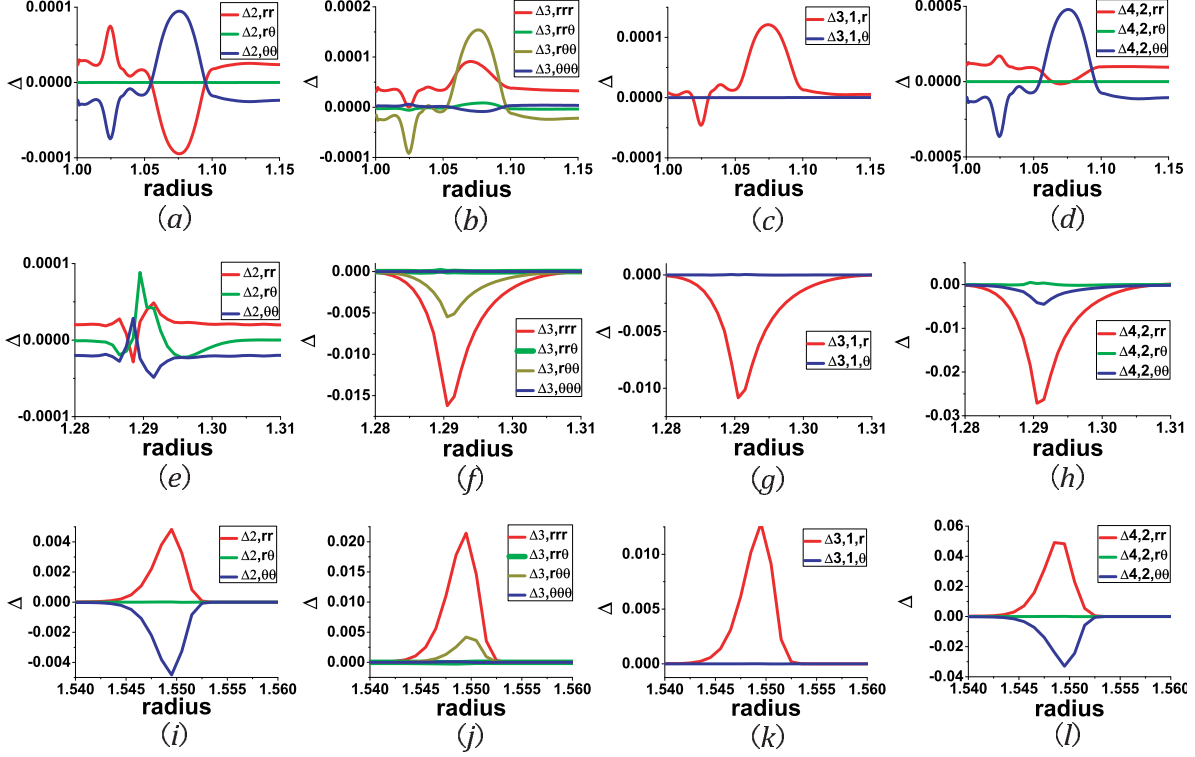


FIG. 17: The deviations Δ_m versus the radius, which are enlargements of the portions labeled by squares in Fig. 16. Figures (a)-(d) are for the region around the first interface, with $1.00 \leq r \leq 1.15$, in Fig.16(e)-(h) respectively. Figures (e)-(h) are for the region around the second interface, with $1.28 \leq r \leq 1.31$. Figures (i)-(l) are for the region around the third interface, with $1.54 \leq r \leq 1.56$.

portions labeled by the 12 squares in Fig.18. The specific correspondences between Figs.19 and 18 are similar to the case of Figs.17 and 16. For the case with sinusoidal perturbation at the material interface, along the same radius, the results of \mathbf{M}_m and Δ_m are shown in Fig.20 and Fig.21. The results of \mathbf{M}_m^* and Δ_m^* are shown in Fig.22 and Fig.23. The specific correspondences between Figs.21 and 20 and the specific correspondences between Figs.23 and 22 are also similar to the case of Figs.17 and 16.

For both the two cases, one can clearly find the existence of the three interfaces via typical variations of the moments and corresponding moment differences. Around the interface for the shock wave, the system starts to deviate from thermodynamic equilibrium once the density starts to increase and goes back to its thermodynamic equilibrium as the density attains its steady value required by the Hugoniot relations. During the procedure deviating from thermodynamic equilibrium, $\Delta_{2,rr}$ (or $\Delta_{2,rr}^*$) shows a positive peak, while $\Delta_{2,\theta\theta}$ (or

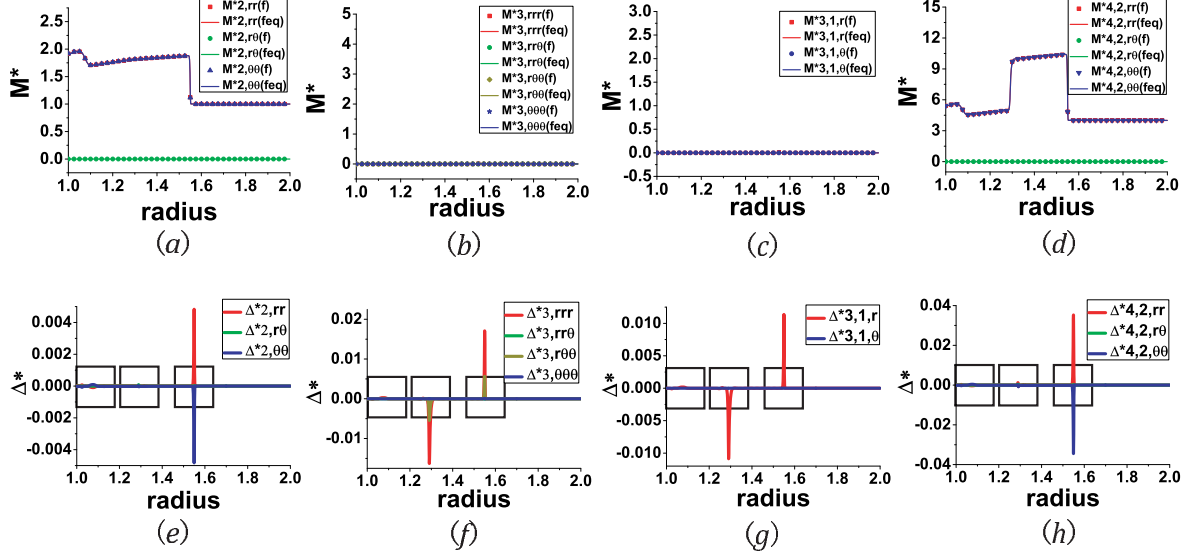


FIG. 18: Central moments and their corresponding non-equilibrium manifestations for the case without perturbation at the material interface. The time $t = 0.15$. Figures (a)-(d) are for \mathbf{M}_2^* , \mathbf{M}_3^* , $\mathbf{M}_{3,1}^*$, $\mathbf{M}_{4,2}^*$, respectively. The symbols are for central moments from f_{ki} and the solid lines are for central moments from f_{ki}^{eq} . Figures (e)-(h) are for deviations Δ_2^* , Δ_3^* , $\Delta_{3,1}^*$, $\Delta_{4,2}^*$, respectively. Only independent components of \mathbf{M}_m^* and Δ_m^* are shown. The specific correspondences are referred to the legends. Three squares are shown to guide the eyes for the interfaces.

$\Delta_{2,\theta\theta}^*$) shows a negative peak with the same amplitude. For this interface, $\Delta_{2,r\theta}$ or $\Delta_{2,r\theta}^*$ is nearly zero. For the material interface, we can find two typical features. The peak value of $\Delta_{2,rr}$ or $\Delta_{2,rr}^*$ here is significantly smaller than that in the case with shock interface. The peak value of $\Delta_{2,r\theta}$ or $\Delta_{2,r\theta}^*$ is larger than that of $\Delta_{2,rr}$ or $\Delta_{2,rr}^*$. The physical reason is as below. The shocking process is very quick, the shock interface is very thin. The changing rates of macroscopic quantities are very high. The system has very little time to relax to its thermodynamic equilibrium and has also very little time for the thermo diffusion. In contrast, due to the thermo diffusion with time, the material interface becomes wider and the system has enough time to relax to its thermodynamic equilibrium. During this procedure, the shear viscosity begins to play a role. Both the shock and rarefaction interfaces are mainly affected by mechanical effects, instead of the thermo diffusion. But the interface of rarefaction wave is much wider than that of the shock wave. Therefore, we can find that the system is much closer to its thermodynamic equilibrium around the rarefaction wave than around the shock wave. $\mathbf{M}_{4,2}$ and $\Delta_{4,2}$ ($\mathbf{M}_{4,2}^*$ and $\Delta_{4,2}^*$) show similar behavior with \mathbf{M}_2 and

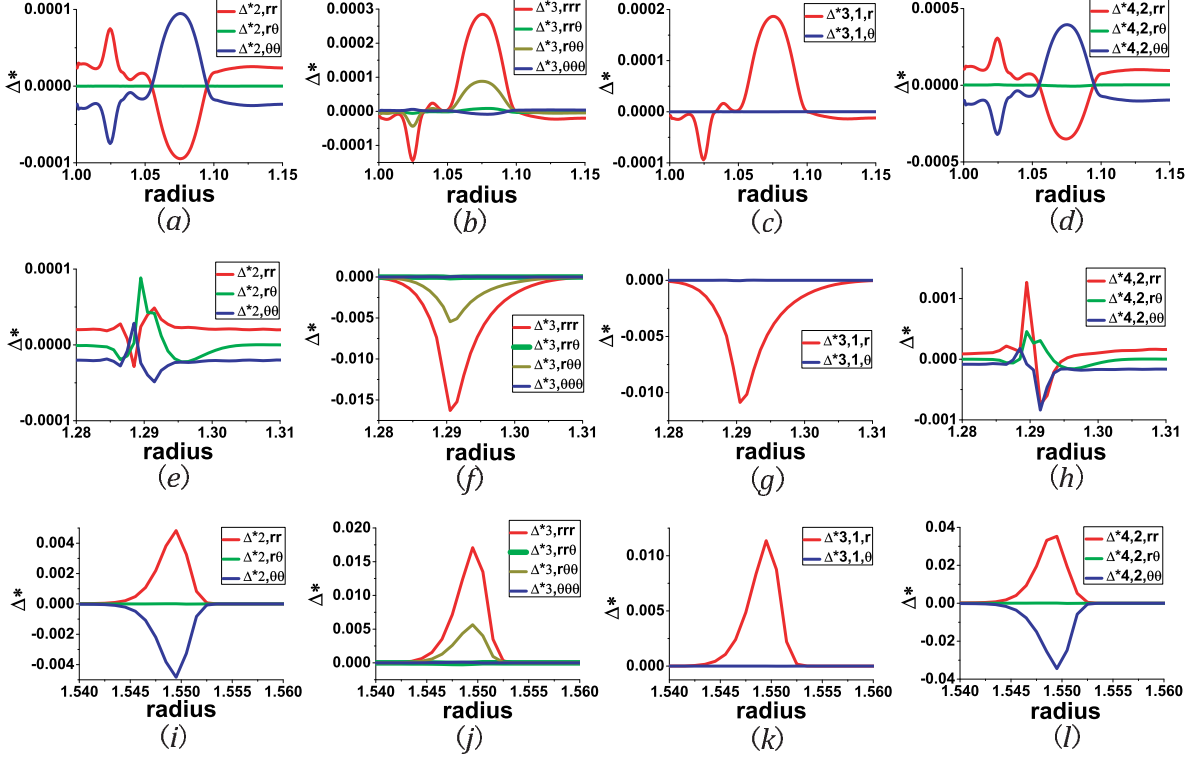


FIG. 19: The deviations Δ_m^* versus the radius, which are enlargements of the portions labeled by squares in Fig. 18. Figures (a)-(d) are for the region around the first interface, with $1.00 \leq r \leq 1.15$, in Fig.18(e)-(h) respectively. Figures (e)-(h) are for the region around the second interface, with $1.28 \leq r \leq 1.31$. Figures (i)-(l) are for the region around the third interface, with $1.54 \leq r \leq 1.56$.

Δ_2 (M_2^* and Δ_2^*). Results of Δ_3^* and $\Delta_{3,1}^*$ can be analyzed in a similar way. The components of Δ_m^* can be labeled by $r^p\theta^q$, where $p, q = 1, 2, \text{ or } 3$. At the shock or rarefaction interface, if $q = 0$, the corresponding component is the largest. If $q = 1$ or 3 , the corresponding component is negligibly small.

Via comparing Fig.17(a) and Fig.21(a) we can find that, the initial perturbation on the material interfaces enhances the shear viscosity effects. Other subfigures in Fig.17 and those in Fig.21 show consistent information. The information from Δ_m in Fig.17 (Fig.21) and that from Δ_m^* Fig.19 (Fig.23) are complimentary.

Via comparing the interfaces for the shock and for the rarefaction in Figs.16-23, we can find that the shock wave increases density, pressure and temperature, while the rarefaction wave decreases those quantities. In other words, the two waves have opposite mechanical effects. Although around both the two interfaces, from left to right, the density value becomes

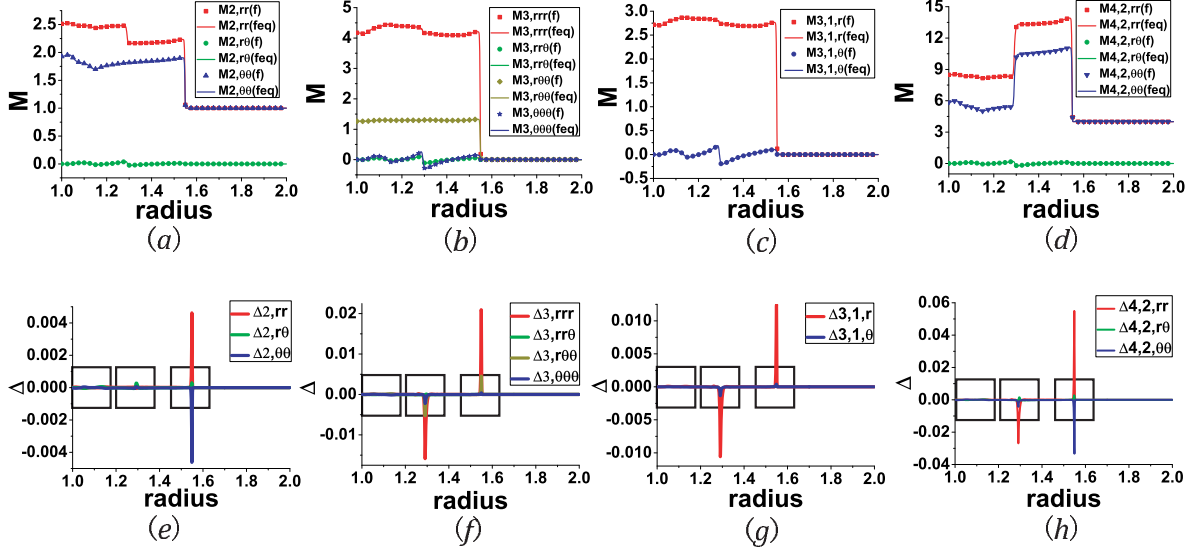


FIG. 20: Moments and their corresponding non-equilibrium manifestations for the case with initial sinusoidal perturbation at the material interface. The time $t = 0.15$. Figures (a)-(d) are for \mathbf{M}_2 , \mathbf{M}_3 , $\mathbf{M}_{3,1}$, $\mathbf{M}_{4,2}$, respectively. The symbols are for moments from f_{ki} and the solid lines are for moments from f_{ki}^{eq} . Figures (e)-(h) are for deviations Δ_2 , Δ_3 , $\Delta_{3,1}$, $\Delta_{4,2}$, respectively. Only independent components of \mathbf{M}_m and Δ_m are shown. The specific correspondences are referred to the legends. Three squares are shown to guide the eyes for the interfaces.

smaller, the non-equilibrium manifestations are oppositely different. The physical reason is as follows. The shock wave propagates outwards, while the rarefaction wave propagates inwards. Along their propagation directions, the temperature decreases around the shock wave, while it increases around the rarefaction wave. Via comparing the moments and corresponding deviations for the two mechanical interfaces and those for the material interface, we can find that the latter shows a great difference in the non-equilibrium manifestations. The shear viscous effects are much more pronounced around the material interface.

All the non-equilibrium effects in Figs.16-23 can be consistently interpreted as below. Among the four physical fields for the density, momentum, pressure and temperature, the temperature gradient is the most fundamental driving force triggering the non-equilibrium effects. The gradient of any other quantity triggers the non-equilibrium effects via triggering macroscopic transportation which leads to temperature gradient. The temperature gradient first initiates variance of the internal kinetic energy in the degree of freedom corresponding to the direction of the temperature gradient. (In this case the temperature shows gradient

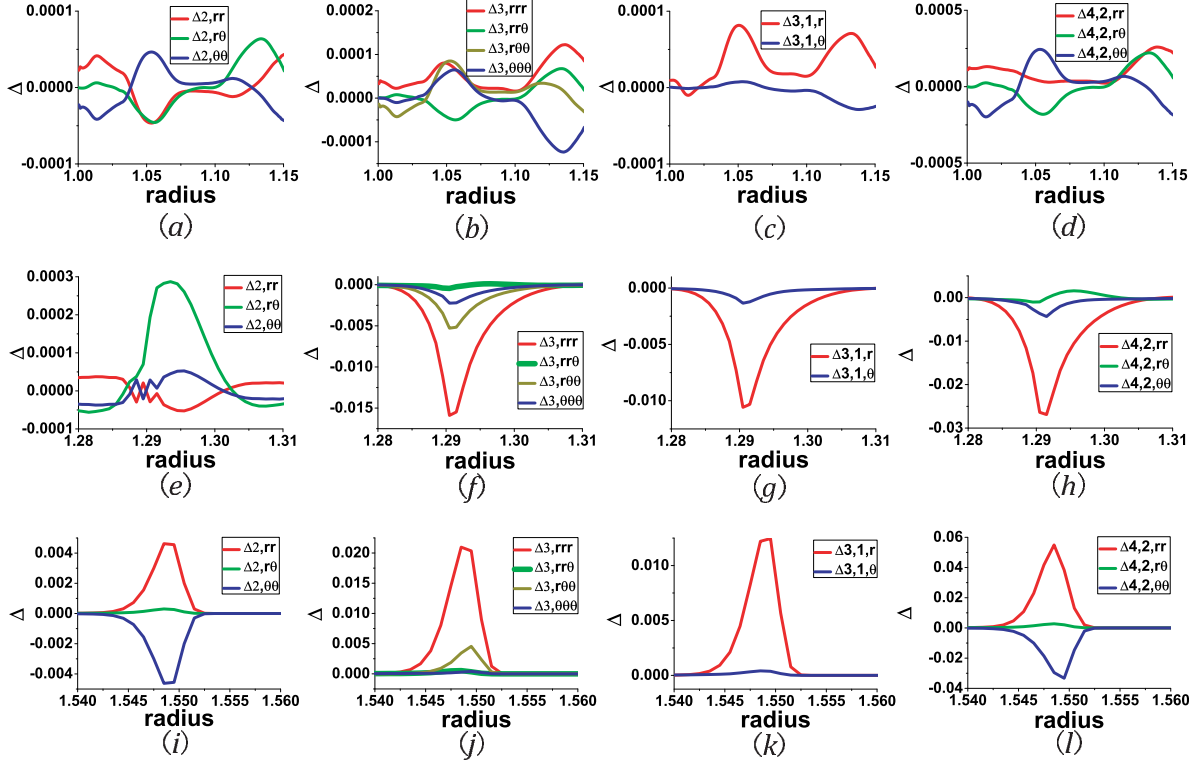


FIG. 21: The deviations Δ_m versus the radius, which are enlargements of the portions labeled by squares in Fig. 20. Figures (a)-(d) are for the region around the first interface, with $1.00 \leq r \leq 1.15$, in Fig.20(e)-(h) respectively. Figures (e)-(h) are for the region around the second interface, with $1.28 \leq r \leq 1.31$. Figures (i)-(l) are for the region around the third interface, with $1.54 \leq r \leq 1.56$.

in the radial direction. This gradient first initiates the variance of the mean kinetic energy $\int d\mathbf{v} f(v_r - u_r)^2/2$.) Then, part of internal kinetic energy variance is transferred to other degrees of freedoms via collisions of molecules. Then, the internal kinetic energy in this degree of freedom further varies according to the temperature gradient, and so on. Only when the temperature gradient vanishes, the system can attain its thermodynamic equilibrium, i.e. the internal kinetic energy in different degrees of the freedom equal to each other.

B. Recovering of the distribution function

When the system is in its thermodynamic equilibrium state, the distribution function of the particle velocity is a local Maxellian, i.e. a normal distribution, symmetric about the mean flow velocity \mathbf{u} , whose variance is proportional to the fluid temperature. These

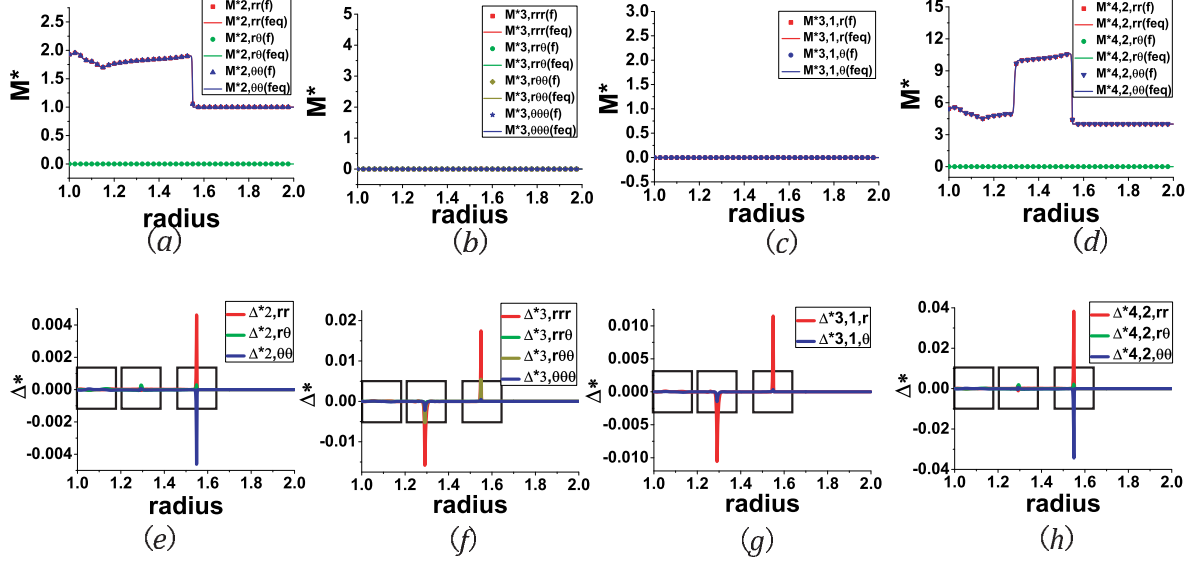


FIG. 22: Central moments and their corresponding non-equilibrium manifestations for the case with initial sinusoidal perturbation at the material interface. The time $t = 0.15$. Figures (a)-(d) are for M_2^* , M_3^* , $M_{3,1}^*$, $M_{4,2}^*$, respectively. The symbols are for central moments from f_{ki} and the solid lines are for central moments from f_{ki}^{eq} . Figures (e)-(h) are for deviations Δ_2^* , Δ_3^* , $\Delta_{3,1}^*$, $\Delta_{4,2}^*$, respectively. Only independent components of M_m^* and Δ_m^* are shown. The specific correspondences are referred to the legends. Three squares are shown to guide the eyes for the interfaces.

properties reflect profound symmetries of Newtonian mechanics, i.e. Galilean and scaling invariance, respectively. The local Maxwellian does not support any dissipative and transport mechanism, since these phenomena violate the aforementioned symmetries. Indeed, transport phenomena triggered by departures from local equilibria reflect into symmetry-breaking departures from the Maxwellian distribution. The maxwellian distribution is shown in Fig.24.

From the results of the LB simulation, via the components of the deviations Δ_m^* , we can draw qualitative information on the actual distribution function. As an example, we consider the case without perturbation at the material interface, and recover qualitatively the actual distribution function. The main steps are given below.

We first consider the actual functions $f(v_r)$ and $f(v_\theta)$ at the leftmost interface, the rarefaction wave. It's easy to find in Fig.19(a) that $\Delta_{2,rr}^*$ shows a negative peak and $\Delta_{2,\theta\theta}^*$ shows a positive peak with the same amplitude. Up to this step, we can imagine that the

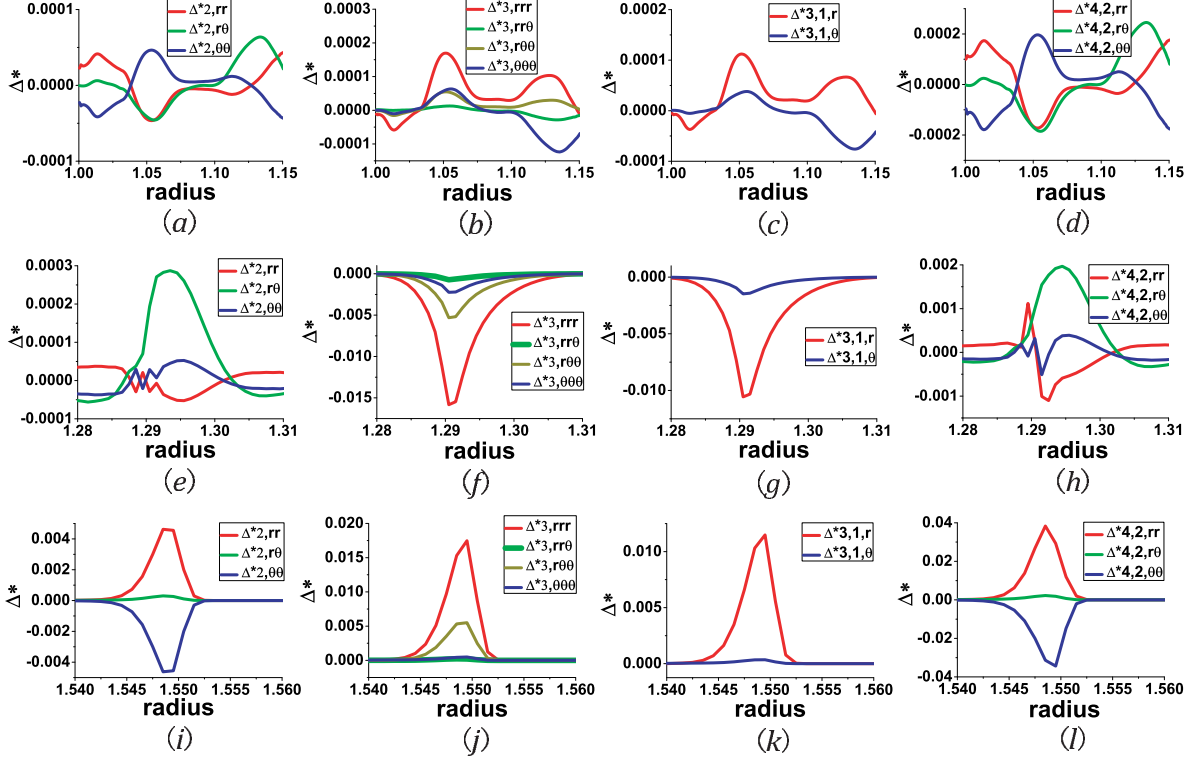


FIG. 23: The deviations Δ_m^* versus the radius, which are enlargements of the portions labeled by squares in Fig. 22. Figures (a)-(d) are for the region around the first interface, with $1.00 \leq r \leq 1.15$, in Fig.22(e)-(h) respectively. Figures (e)-(h) are for the region around the second interface, with $1.28 \leq r \leq 1.31$. Figures (i)-(l) are for the region around the third interface, with $1.54 \leq r \leq 1.56$.

distribution function $f(v_r)$ is “thinner” and $f(v_\theta)$ is “fatter” than the Maxwellian. The peak of $f(v_r)$ is higher and the peak of $f(v_\theta)$ is lower than that of the Maxwellian. $\Delta_{4,2}^*$ in Fig.19 (d) shows complementary information to Δ_2^* in Fig.19(a). According to Δ_3^* in Fig.19(b) and $\Delta_{3,1}^*$ in Fig.19(c), we can obtain that $f(v_\theta)$ is symmetric, while the $f(v_r)$ is asymmetric. The portion for $v_r > 0$ is “fatter” than that for $v_r < 0$. This is often called “positive skewness”. A sketch of the actual distribution functions, $f(v_r)$ and $f(v_\theta)$, are shown in Fig.25 (a), where the dashed line shows the Maxwellian which is for both $f^{eq}(v_r)$ and $f^{eq}(v_\theta)$. A sketch of the distribution functions around the shock wave is shown in Fig.25(c), where $f(v_r)$ is “fatter” and $f(v_\theta)$ is “thinner” than the Maxwellian. The peak of $f(v_r)$ is lower and the peak of $f(v_\theta)$ is higher than that of the Maxwellian and $f(v_\theta)$ is symmetric, while $f(v_r)$ is asymmetric. The portion for $v_r > 0$ is “fatter” and the portion for $v_r < 0$ is “thinner”. Similarly, we can obtain the sketch of actual distribution function around the materia interface. See Fig.25(b).

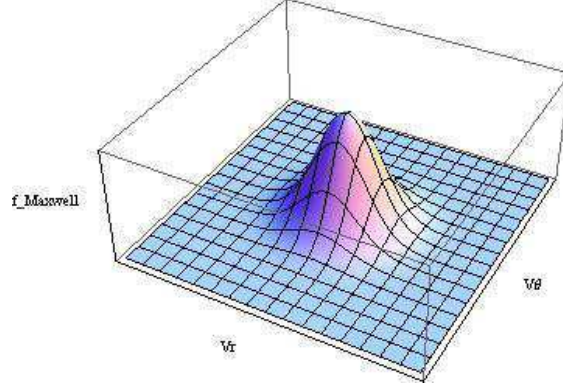


FIG. 24: The sketch of the Maxwellian distribution function in velocity space (v_r, v_θ) .

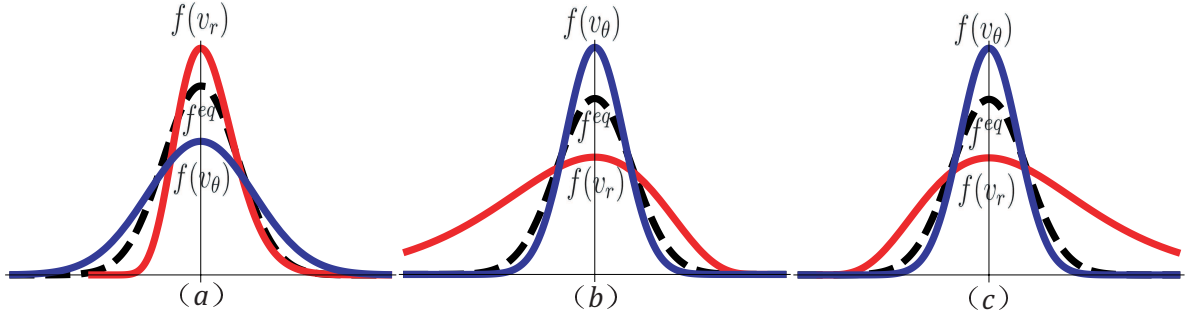


FIG. 25: The sketch of the Maxwellian and actual distribution functions versus velocity v_r and v_θ , respectively. Figure (a) shows the distribution functions at the interface for rarefaction wave, Fig.(b) shows the ones at the material interface and Fig.(c) is for those at the interface for shock wave. The red solid line is for distribution function $f(v_r)$, the blue solid one is for distribution function $f(v_\theta)$, and the dashed line is for f^{eq} .

Secondly, we study the contours of the actual distribution function in two-dimensional velocity space (v_r, v_θ) . It's clear that the values of $\Delta_{2,r\theta}^*$ in Fig.19 (a) and Fig.19 (i) equal to zero, which implies that the contours of the actual distribution function at the rarefaction and the shock waves ought to be symmetric in v_r or/and v_θ . With in mind that $f(v_\theta)$ is symmetric at the two interfaces, we can confirm that the v_r coordinate axis is the symmetric axis for the contour. Figures 19(d) and (l) show consistent information. $\Delta_{2,r\theta}^*$ in Fig.19 (e) shows a positive peak, which implies that, at the material interface, the contour is not symmetric around the v_r or v_θ coordinate. Because the shear viscous effects are pronounced, the actual distribution function is relatively complex. Figure 26 shows, from left to right, the sketches of contours of the actual distribution function at the interfaces of rarefaction,

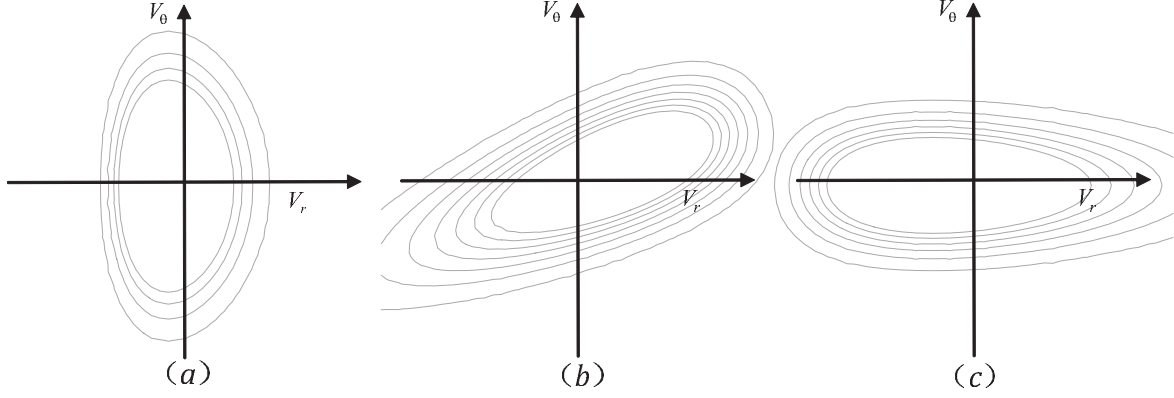


FIG. 26: The sketch of contours of the actual distribution functions in velocity space (v_r, v_θ) . Figure (a)-(c) show the recovered distribution function contours at the three interfaces, rarefaction wave, material interface and shock wave, respectively.

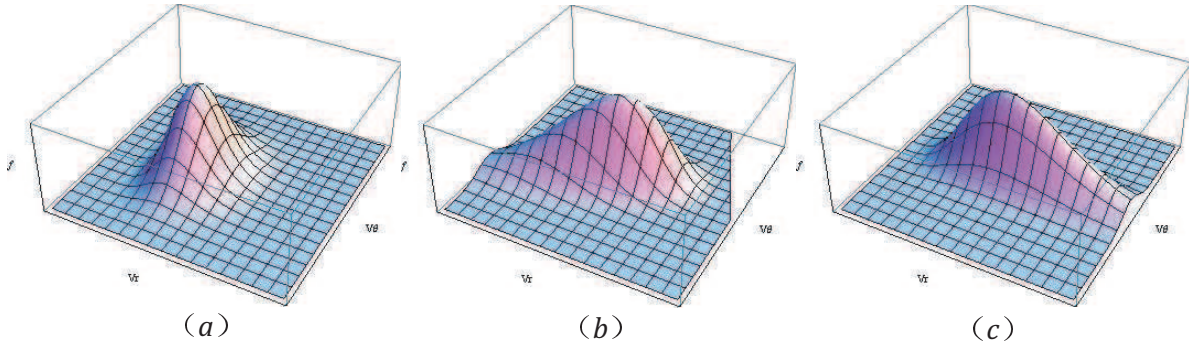


FIG. 27: The sketches of the actual distribution functions in velocity space (v_r, v_θ) . Figures (a)-(c) show the recovered distribution functions at the three interfaces, rarefaction wave, material interface and shock wave, respectively.

material and shock.

Finally, by combining the results of the above two steps, we obtain the qualitative curves for the actual distribution functions at the three interfaces. The sketches are shown in Fig.27. Figures (a)-(c) are for the rarefaction wave, the material interface and the shock wave, respectively.

V. CONCLUSIONS AND DISCUSSIONS

A polar coordinate lattice Boltzmann model for compressible flows is presented. The key technique in this model is an operator-splitting scheme for the temporal and spatial evolutions. The convection term is solved via a modified Warming-Beam scheme where a switch function is introduced. The temporal evolution is calculated analytically. The new model works for both subsonic and supersonic flows, and consequently, it can be used to study complex flows under strong impact or shock. The new model is validated and verified via typical benchmark tests. For example, (i) the rotational slip flow, (ii) the Kelvin-Helmholtz(KH) instability, (iii) the stable shock tube problem, (iii) the Richtmyer-Meshkov(RM) instability. The latter two can not be simulated by the previous PCLB model[45]. Even for the former two cases where the previous model[45] works, the simulation results by the new model appear to be more accurate. Choosing computational domain and designing boundary conditions play an important role in numerical experiments. For annular systems showing periodic behaviors in the circumferential direction, one can pick out only one period of the domain for simulations. In such a case, the two boundaries in the circumferential direction are treated with periodic conditions. On the other hand, the two boundaries in the radial direction should be treated carefully according to the specific situation under investigation. The simplest microscopic radial boundary conditions assume that the system at the inner and outer boundaries are in thermodynamic equilibrium. More accurate distribution functions at the radial boundaries take into account the part deviating from equilibrium, which can be obtained via interpolation schemes from values at the neighboring lattice nodes inside the system.

To show the merit of the PCLB model over the traditional methods based on hydrodynamics, we studied the macroscopic behaviors of the system resulted from departures from thermodynamic equilibrium around three kinds of interfaces, the shock wave, the rarefaction wave and the material interface, for two specific cases. In one of the two cases, the material interface is initially perturbed and consequently the RM instability occurs. It is found that, the macroscopic effects of deviating from thermodynamic equilibrium at the material interface are greatly different from those at the mechanical interfaces. The coupling effects of the molecular thermal motions in different degrees of freedom are much more pronounced at the material interface. The initial perturbation at the material interface results in more

pronounced two-dimensional effects and enhanced coupling effects of molecular motions in different degrees of freedom. The amplitude of deviating from equilibrium at the shock wave is much higher than those at the rarefaction wave and material interface. The above numerical results confirm that the temperature increase first initiates the increase of internal kinetic energy in the degree of freedom corresponding to the direction of temperature gradient, then increases those in other degrees of freedom, and vice versa. By comparing each component of the high-order moments and its value in equilibrium, we can draw qualitative information on the actual distribution function. These results deepen our understanding on the mechanical and material interfaces from a more fundamental point of view, and present valuable information to improve the physical modeling at the macroscopic level. Work based on the current LB model for systematic investigations of non-equilibrium effects in the RM instability and KH instability, is in progress.

Acknowledgements

The authors thank Prof. Guoxi Ni for many helpful discussions. AX and GZ acknowledge support of the Science Foundations of CAEP [under Grant Nos. 2012B0101014 and 2011A0201002] and the Foundation of State Key Laboratory of Explosion Science and Technology. AX, GZ, YL and CL acknowledge support of National Natural Science Foundation of China [under Grant Nos. 11075021, 11074300, and 91130020].

-
- [1] S. Succi, *The Lattice Boltzmann Equation for Fluid Dynamics and Beyond*, Oxford University Press, New York, (2001).
 - [2] F. J. Alexander, H. Chen, S. Chen and G. D. Doolen, Phys. Rev. A 46, 1967 (1992).
 - [3] G. W. Yan, Y. S. Chen, S. X. Hu, Phys. Rev. E 59, 454 (1999).
 - [4] C. H. Sun, Phys. Rev. E 58, 7283 (1998).
 - [5] C. Sun and A. T. Hsu, Phys. Rev. E 68, 016303 (2003).
 - [6] N. Cao, S. Chen, S. Jin, and D. Martinez, Phys. Rev. E 55, R21 (1997).
 - [7] T. Kataoka and M. Tsutahara, Phys. Rev. E 69, 056702 (2004).
 - [8] T. Kataoka and M. Tsutahara, Phys. Rev. E 69, 035701(R)(2004).

- [9] M. Watari and M. Tsutahara, Phys. Rev. E 67, 036306 (2003).
- [10] M. Watari and M. Tsutahara, Phys. Rev. E 70, 016703 (2004).
- [11] M. Watari, Physica A 382, 502 (2007).
- [12] A. Xu, Phys. Rev. E 71, 066706 (2005).
- [13] A. Xu, Europhys. Lett. 69, 214 (2005).
- [14] A. Xu, G. Gonnella, and A. Lamura, Phys. Rev. 67, 056105 (2003).
- [15] A. Xu, G. Gonnella, and A. Lamura, Phys. Rev. E 74, 011505 (2006).
- [16] A. Xu, G. Gonnella, A. Lamura, G. Amati, and F. Massaioli, Europhys. Lett. 71, 651 (2005).
- [17] A. Xu, G. Zhang, Y. Gan, F. Chen, and X. Yu, Front. Phys. 7(5), 582 (2012)
- [18] Y. Li, R. Shock, R. Zhang, and H. Chen, J. Fluid Mech. 519, 273 (2004).
- [19] X.F. Pan, A.G. Xu, G.C. Zhang, and S. Jiang, Int. J. Mod. Phys. C 18, 1747 (2007).
- [20] Y. Gan, A. Xu, G. Zhang, and Y. Li, Commun. Theor. Phys. 50, 201 (2008).
- [21] Y. Gan, A. Xu, G. Zhang, X. Yu, and Y. Li, Physica A 387, 1721 (2008).
- [22] Y. Gan, A. Xu, G. Zhang, and Y. Li, Commun. Theor. Phys. 56, 490 (2011).
- [23] Y. Gan, A. Xu, G. Zhang, and Y. Li, Phys. Rev. E 83, 056704 (2011).
- [24] Y. Gan, A. Xu, G. Zhang, Y. Li and H. Li, Phys. Rev. E 84, 046715 (2011).
- [25] Y. Gan, A. Xu, G. Zhang, and Y. Li, Europhys. Lett. 97, 44002 (2012).
- [26] Y. Gan, A. Xu, G. Zhang, and Y. Li, Front. Phys. 7(4), 481 (2012)
- [27] F. Chen, A. Xu, G. Zhang, Y. Gan, C. Tao, and Y. Li, Commun. Theor. Phys. 52, 681 (2009).
- [28] F. Chen, A. Xu, G. Zhang, Y. Li, S. Succi, EuroPhys. Lett. 90, 54003 (2010).
- [29] F. Chen, A. Xu, G. Zhang, Y. Li, Commun. Theor. Phys. 54, 1121, (2010).
- [30] F. Chen, A. Xu, G. Zhang, Y. Li, Commun. Theor. Phys. 55, 325 (2011).
- [31] F. Chen, A. Xu, G. Zhang, Y. Li, Phys. Lett. A 375, 2129 (2011).
- [32] F. Chen, A. Xu, G. Zhang, Y. Li, Commun. Theor. Phys. 56, 333, (2011).
- [33] F. Chen, A. Xu, G. Zhang, Y. Li, Theor. & Appl. Mech. Lett. 1, 052004 (2011).
- [34] F. Nannelli, S. Succi, J. Stat. Phys. 68, 401 (1992).
- [35] Succi, Amati and Benzi, J. Stat. Phys. 81, 5 (1995).
- [36] Amati, Succi and Benzi, Fluid Dyn. Res. 19, 289 (1997).
- [37] G. Peng, H. Xi, C. Duncan and S. Chou, Phys. Rev. E 58, R4125 (1998).
- [38] G. Peng, H. Xi C. Duncan and S. Chou, Phys. Rev. E 59, 4676 (1999)
- [39] S. Ubertini, G. Bella and S. Succi, Phys. Rev. E 68, 016701 (2003)

- [40] X. He, G. Doolen, J. Comput. Phys. 134, 306 (1997).
- [41] R. Mei, W. Shyy, J. Comput. Phys. 143, 426 (1998).
- [42] I. Halliday, L. A. Hammond, C. M. Care, K. Good, and A. Stevens, Phys. Rev. E 64, 011208 (2001).
- [43] K. N. Premnath and J. Abraham, Phys. Rev. E 71, 056706 (2005).
- [44] P. Asinari, S. C. Mishra and R. Borchellini, Numerical Heat Transfer B 57, 126 (2010).
- [45] M. Watari, Commun. Comput. Phys. 9, 1293 (2011).
- [46] P. Bhatnagar, E. P. Gross, and M. K. Krook, Phys. Rev. 94, 511 (1954).
- [47] R. D. Richtmyer, Comm. Pure Appl. Math. 13, 297 (1960).
- [48] E. E. Meshkov, Sov. Fluid Dyn. 4, 101 (1969).
- [49] R. F. Benjamin, *Advances in Compressible Turbulent Mixing*, edited by W. P. Dannevik, A. C. Buckingham, and C. E. Leith (1992).
- [50] Q. Zhang and S. Sohn, Phys. Fluids 9, 1106 (1997).